Jang and Nakamura
The Journal of Headache and Pain (2025) 26:42
https://doi.org/10.1186/s10194-025-01968-7

The Journal of Headache and Pain

RESEARCH

Open Access

Pregnenolone sulfate potentiates tetrodotoxin-resistant Na^+ channels to increase the excitability of dural afferent neurons in rats

Il-Sung Jang[1,2*] and Michiko Nakamura[2*]

Abstract

Background Although peripheral administration of pregnenolone sulfate (PS) has been reported to produce pronociceptive effects, the mechanisms by which PS modulates the excitability of nociceptive neurons are poorly understood. Here, we report on the excitatory role of PS in peripheral nociceptive neurons, focusing on its effects on tetrodotoxin-resistant (TTX-R) Na^+ channels.

Methods TTX-R Na^+ current (I_{Na}) mediated by $Na_V1.8$ was recorded from acutely isolated small-sized dural afferent neurons of rats, identified with the retrograde fluorescent dye DiI, using a whole-cell patch-clamp technique.

Results Transcripts for enzymes and transporters involved in PS biosynthesis were detected in the ophthalmic branch of the trigeminal ganglia. In voltage-clamp mode, PS preferentially potentiated the TTX-R persistent I_{Na}, a small non-inactivating current during sustained depolarization. PS shifted the voltage-inactivation relationship toward a depolarizing range. PS also delayed the onset of inactivation and accelerated the recovery from inactivation of TTX-R Na^+ channels. Additionally, PS decreased the extent of use-dependent inhibition of TTX-R Na^+ channels. In current-clamp mode, PS hyperpolarized dural afferent neurons by increasing the leak K^+ conductance. Nevertheless, PS decreased the rheobase current—the minimum current required to generate action potentials—and increased the number of action potentials elicited by depolarizing current stimuli.

Conclusion We have shown that the excitatory neurosteroid PS preferentially potentiates TTX-R persistent I_{Na} and reduces the inactivation of TTX-R Na^+ channels, resulting in increased excitability of dural afferent neurons. The potential role of endogenous PS in migraine pathology warrants further investigation.

Introduction

Neurosteroids are endogenous steroid-related substances that affect neuronal functions by modulating various receptors and ion channels [1]. They are either synthesized directly within the central and peripheral nervous systems or transported to nervous tissues through the bloodstream after synthesis in endocrine glands [1]. Neurosteroids are largely classified into inhibitory—such as allopregnanolone and tetrahydrodeoxycorticosterone—and excitatory, including pregnenolone sulfate (PS), dehydroepiandrosterone (DHEA), and DHEA sulfate (DHEAS) [2, 3]. Of these, PS has been implicated in several pathological conditions related to excessive

*Correspondence:
Il-Sung Jang
jis7619@knu.ac.kr
Michiko Nakamura
michiko21a@gmail.com
[1] Department of Pharmacology, School of Dentistry, Kyungpook National University, 2177 Dalgubeol-daero, Jung-gu, Daegu 41940, Republic of Korea
[2] Brain Science & Engineering Institute, Kyungpook National University, 2177 Dalgubeol-daero, Jung-gu, Daegu 41940, Republic of Korea

neuronal excitability, including epilepsy [4], because it exerts excitatory effects in central neurons via inhibition of inhibitory $GABA_A$ receptors [5, 6], potentiation of excitatory NMDA receptors [7, 8], and enhancement of glutamatergic synaptic transmission [9–11]. PS is also closely involved in nociceptive transmission in peripheral tissues. For example, the intradermal application of PS stimulates nociceptor endings to elicit nociceptive flexor responses in mice via activation of σ1 receptors [12]. Additionally, intraplantar injection of PS into the skin of the hind paw evokes nocifensive responses by activating transient receptor potential melastatin 3 (TRPM3), a non-selective cation channel [13]. Furthermore, PS, via activation of TRPM3, increases the release of calcitonin gene-related peptide, which is a key molecule involved in migraine pathology through the induction of neurogenic inflammation in the trigeminovascular system of the dura mater [14–16].

Of the nine subtypes of voltage-gated Na^+ channels ($Na_V1.1$ to $Na_V1.9$), the tetrodotoxin (TTX)-sensitive $Na_V1.7$ and TTX-resistant (TTX-R) $Na_V1.8$ and $Na_V1.9$ are specifically expressed in nociceptive sensory neurons [17]. In particular, $Na_V1.8$ has been implicated in inflammatory hyperalgesia [18], since the representative inflammatory mediator prostaglandin E_2 sensitizes nociceptive neurons by potentiating $Na_V1.8$-mediated current [19, 20]. $Na_V1.8$ and the persistent Na^+ current (I_{NaP}), which is the non-inactivating current during sustained membrane depolarization, mediated by this channel subtype have been suggested as potential pharmacological targets for treating migraine headaches because (1) both propranolol, a β-blocker, and amitriptyline, a non-selective serotonin and norepinephrine reuptake inhibitor, which are frequently used for migraine prevention, preferentially inhibit TTX-R I_{NaP} [21, 22], and (2) the density of TTX-R I_{NaP} is increased in dural afferent neurons treated with a mixture of inflammatory mediators [23]. Furthermore, a recent study has shown that the selective I_{NaP} inhibitor GS-967 reduces pain behavior in an animal model of migraine headache [24].

In the present study, we explored a possible relationship between migraine pathology and neurosteroids by examining the modulation of TTX-R Na^+ channels by neurosteroids. Key enzymes involved in steroidogenesis are expressed in various tissues involved in nociceptive signal transduction [25–27], suggesting that locally generated neurosteroids may affect the excitability of central as well as peripheral neurons. To the best of our knowledge, this is the first study showing that the neurosteroid PS positively modulates TTX-R Na^+ channels, particularly TTX-R I_{NaP}, to increase the excitability of dural afferent neurons identified with the retrograde fluorescent dye DiI.

Materials and methods

Preparation

All experiments were conducted in accordance with animal protocols approved by the Animal Care Committee of Kyungpook National University (Approval No. KNU-2023-0212). Animal studies are reported in compliance with the ARRIVE guidelines [28], and every effort was made to minimize both the number of animals used and their suffering.

Neurons within the trigeminal ganglia (TG) innervating the dura were identified after application of the retrograde tracer DiI to the dura, as previously described [29, 30]. Briefly, male Sprague–Dawley rats (3–4 weeks old; Samtako, Osan, Republic of Korea) were intraperitoneally anesthetized with a mixture of ketamine (20 mg/kg) and xylazine (10 mg/kg). The cranial bone overlying the superior sagittal sinus was gently removed using a dental drill in a careful craniotomy procedure, exposing the dura. Ten microliters of DiI solution—prepared by diluting 100 mg/mL DiI in DMSO (dimethyl sulfoxide) 1:10 (v/v) with saline—was applied to the dura. One minute after applying the DiI solution, dental resin was placed on the exposed dura to replace the removed cranial bone. The incision was closed with sutures, and the rats received intramuscular injections of penicillin G (100,000 U/kg) and naproxen (10 mg/kg) to reduce postoperative infection and pain. At 7–10 days after the DiI application, the rats were decapitated under ketamine anesthesia (50 mg/kg, intraperitoneally). Pairs of ophthalmic branch of the TG were dissected and treated with a standard external solution [in mM: 150 NaCl, 5 KCl, 2 $CaCl_2$, 1 $MgCl_2$, 10 glucose, and 10 HEPES (pH 7.4 with Tris-base)] containing 0.3% collagenase (type I) and 0.3% trypsin (type I) for 40–60 min at 37 °C. Thereafter, TG neurons were mechanically dissociated using trituration with fire-polished Pasteur pipettes in a culture dish (Primaria 3801; Becton Dickinson, Rutherford, NJ, USA). The isolated neurons were used for electrophysiological recordings 2–6 h after preparation.

Electrical measurements

All electrical measurements were performed using conventional whole-cell patch-clamp recordings and a standard patch-clamp amplifier (MultiClamp 700B; Molecular Devices, Union City, CA, USA). Neurons were voltage-clamped at a holding potential of −80 mV, except where indicated. Patch pipettes were made from borosilicate capillary glass (G-1.5; Narishige, Tokyo, Japan) using a

pipette puller (P-97; Sutter Instrument Co., Novato, CA, USA). The resistance of the recording pipettes filled with the internal solution was 0.7–1.0 MΩ. Membrane potentials were corrected for the liquid junction potential, and pipette capacitance and series resistance (40–80%) were compensated. DiI-positive TG neurons were viewed under phase contrast or fluorescence on an inverted microscope (T*i*; Nikon, Tokyo, Japan). Membrane currents were filtered at 3–10 kHz, digitized at 20–50 kHz (except where indicated), and stored on a computer equipped with pCLAMP software (version 10.7, Molecular Devices).

In voltage-clamp experiments, TTX-R Na^+ current (I_{Na}) was isolated using a bath solution composed of the following (in mM): 130 NaCl, 20 tetraethylammonium-Cl, 2 $CaCl_2$, 1 $MgCl_2$, 10 HEPES, 10 glucose, 0.0003 TTX, and 0.1 $CdCl_2$ (pH 7.4 with Tris-base). The pipette solution contained (in mM): 140 CsF, 10 CsCl, 2 EGTA, 2 ATP-Na_2, and 10 HEPES (pH 7.2 with Tris-base). To record voltage-gated K^+ current (I_K), the bath solution contained (in mM): 150 N-methyl-D-glucamine-Cl, 20 CsCl, 2 $CaCl_2$, 1 $MgCl_2$, 10 HEPES, 10 glucose, 0.0003 TTX, and 0.1 $CdCl_2$ (pH 7.4 with Tris-base), and the pipette solution contained (in mM): 153 KCl, 2 $CaCl_2$, 1 $MgCl_2$, 10 HEPES, and 10 glucose (pH 7.2 with Tris-base). Capacitance and leak currents were subtracted using the P/4 subtraction protocol (pCLAMP 10.7) to record TTX-R I_{Na} and voltage-gated I_K. In current-clamp experiments, the bath solution was composed of (in mM): 150 NaCl, 5 KCl, 2 $CaCl_2$, 1 $MgCl_2$, 10 HEPES, 10 glucose, and 0.0003 TTX (pH 7.4 with Tris-base), except where indicated, and the pipette solution contained (in mM): 140 KF, 10 KCl, 2 EGTA, 2 ATP-Na_2, and 10 HEPES (pH 7.2 with Tris-base).

RT-PCR

Sprague–Dawley rats (4 weeks old) were decapitated under ketamine anesthesia (100 mg/kg, i.p.), and the ophthalmic branch of TG, liver, testis, and adrenal gland were dissected. The tissues were homogenized using a Taco™Prep Bead Beater (GeneReach Biotechnology Corp., Taipei, Taiwan). Total RNA was extracted from these tissues using Takara MiniBEST Universal RNA Extraction Kit (Takara, Tokyo, Japan) and reverse transcription (RT) was performed by RevertAid First Strand cDNA Synthesis Kit (Thermo Fisher Scientific, Waltham, MA, USA). Subsequently, PCR was performed using the obtained cDNA samples in a PCR thermal cycler (TP350; Takara). The primers used for PCR were as follows: P450scc (164 bp); 5'-gcacacaacttgaaggtacaggag-3'/ 5'-tacctctgcaaggtcacagagatg-3', P450c17 (136 bp); 5'-gtcgtcaatctctgggcact-3'/ 5'-cagctccgaagggcaagtaa-3', 3β-HSD (176 bp); 5'-tctggatgcccagtacctga-3'/ 5/'-agatgaaggctggcacactg-3', SULT2A1 (168 bp); 5'-aaggaccacgactcatgacc-3'/ 5'-ccagtgagtctggcttcttca-3', SULT2B1 (130 bp); 5'-cacctaccccaaatcaggca-3'/ 5'-acttatggtggtctcgcacc-3' STS (187 bp); 5'-ctatggcaaccgcacactca-3'/ 5'-tgccgagaacaggaatacacc-3', OTS-α (181 bp); 5'-attacagcatctcccctgcc-3'/ 5'-ttcttgatggggcaaagggt-3', TSPO (192 bp); 5'-ggaggctatggttcccttg-3'/ 5'-taaggatacagcaagcgggc-3'. The PCR products were visualized on a 1.5% agarose gel, to which RedSafeTM Nucleic Acid Staining Solution had been added, and the gels subsequently photographed.

Data analysis

In voltage-clamp experiments, the peak amplitude of transient TTX-R I_{Na} was measured by subtracting the baseline from the peak amplitude using Clampfit software (version 10.7, Molecular Devices). The amplitude of the steady-state component of transient TTX-R I_{Na} was measured by subtracting the baseline from the mean amplitude at 90–95 ms. The decay phase of TTX-R I_{Na} was best fitted to a triple exponential function using the following equation:

$$I(t) = A_0 + A_{fast} \times [1 - \exp(-t/\tau_{fast})] + A_{intermediate} \times [1 - \exp(-t/\tau_{intermediate})] + A_{slow} \times [1 - \exp(-t/\tau_{slow})],$$

where $I(t)$ is the amplitude of TTX-R I_{Na} at time t, and A_{fast}, $A_{intermediate}$, and A_{slow} are the amplitude fraction of fast, intermediate, and slow time constants (τ_{fast}, $\tau_{intermediate}$, and τ_{slow}), respectively. To investigate the voltage-activation relationship, the amplitude of TTX-R I_{Na} was transformed into conductance (G) using the following equation:

$$G = I/(V\text{-}E_{Na}),$$

where E_{Na} is the Na^+ equilibrium potential calculated using the Nernst equation. The voltage–activation and voltage–inactivation relationships of TTX-R Na^+ channels were fitted to Boltzmann equations:

$$G/G_{max} = 1/\{1 + \exp[(V_{50,activation} - V)/k]\} \text{ and } I/I_{max} = 1 - 1/\{1 + \exp[(V_{50,inactivation} - V)/k]\},$$

where G_{max} and I_{max} are the maximum conductance and current amplitude, respectively; $V_{50,activation}$ and $V_{50,inactivation}$ are the half-maximal voltages for activation and fast inactivation, respectively; and k is the slope factor.

$$R(t) = A_0 + A_{fast} \times [1 - \exp(-t/\tau_{fast})] + A_{intermediate} \times [1 - \exp(-t/\tau_{intermediate})] + A_{slow} \times [1 - \exp(-t/\tau_{slow})],$$

The kinetic data for the development of inactivation were best fitted to a double exponential function:

$$R(t) = A_0 + A_{fast} \times [\exp(-t/\tau_{fast})] + A_{slow} \times [\exp(-t/\tau_{slow})],$$

where $R(t)$ is the amplitude ratio of two TTX-R I_{Na} at time t, and A_{fast} and A_{slow} are the amplitude fractions of τ_{fast} and τ_{slow}, respectively. The kinetic data for the recovery from inactivation were best fitted to a triple exponential function using the following equation:

$$R(t) = A_0 + A_{fast} \times [1 - \exp(-t/\tau_{fast})] + A_{intermediate} \times [1 - \exp(-t/\tau_{intermediate})] + A_{slow} \times [1 - \exp(-t/\tau_{slow})],$$

where $R(t)$ is the amplitude ratio of two TTX-R I_{Na} at time t, and A_{fast}, $A_{intermediate}$, and A_{slow} are the amplitude fraction of τ_{fast}, $\tau_{intermediate}$, and τ_{slow}, respectively. The weighted time constants ($\tau_{weighted}$) for inactivation and recovery kinetics were calculated using:

$$\tau_{weighted} = [(\tau_{fast} \times A_{fast}) + (\tau_{intermediate} \times A_{intermediate}) + (\tau_{slow} \times A_{slow})]/(A_{fast} + A_{intermediate} + A_{slow})$$

or

$$[(\tau_{fast} \times A_{fast}) + (\tau_{slow} \times A_{slow})] / (A_{fast} \times A_{slow}).$$

In current-clamp experiments, the rheobase current—the minimal threshold current to trigger action potentials in patched neurons—was determined by successive depolarizing current stimuli (10 pA increments, 500 ms duration). The number of action potentials elicited by four successive depolarizing current stimuli [multiples of the threshold (T) current (1T to 4T), 1 s duration] was counted in the absence and presence of PS or DHEA. Numerical values are provided as the mean ± standard error of the mean (SEM) using values normalized to the control. Significant differences in the mean amplitudes were tested using Student's paired two-tailed *t*-test or ANOVA with absolute values rather than normalized values. The statistical test method is defined in the relevant figure legends. Values of $p < 0.05$ were considered statistically significant.

Drugs

The following drugs were used in this study: pregnenolone, PS, DHEA, DHEAS, riluzole, collagenase, trypsin, TTX, ononetin, BD-1047, γ-cyclodextrin (γ-CD), capsaicin (Sigma, St. Louis, MO, USA); A-1899 (Tocris, Bristol, England); apamin (MedChemExpress, Monmouth Junction, NJ, USA). All extracellular solutions were applied using the 'Y-tube system' for rapid solution exchange [31]. Neurosteroids were dissolved in dimethyl sulfoxide (DMSO) to give a stock solution of 10 to 300 mM, and the final concentration of DMSO applied to the external solution was ≤0.1% v/v. Application of DMSO alone (0.1% v/v) had no effect of TTX-R I_{Na} (data not shown). It was noted that neurosteroids used in this study have limited solubility in aqueous solutions. For example, pregnenolone, PS, DHEA, and DHEAS were insoluble at final concentrations of ≥100 μM, ≥1 mM, ≥300 μM, and ≥1 mM, respectively. Since the primary focus of the present study was to investigate how PS affects TTX-R Na^+ channels and neuronal excitability, PS was used at concentrations between 10 and 100 μM in most experiments. This concentration range was chosen based on estimates of endogenous PS concentrations found in hippocampal tissue [32].

Results

Expression of enzymes involved in the neurosteroid synthesis in dural afferent neurons

In the neurosteroidergic pathway, cholesterol is firstly metabolized into pregnenolone by the enzyme cytochrome P450 side-chain cleavage (P450scc). Pregnenolone is further metabolized into DHEA and progesterone by steroid 17α-hydroxylase (P450c17) and 3β-hydroxysteroid dehydrogenase (3β-HSD), respectively (Fig. 1A). Pregnenolone and DHEA are further sulfated by sulfotransferases (SULTs), such as the SULT2A1 and SULT2B1 subtypes (Fig. 1A). Before investigating the effects of neurosteroids on TTX-R Na^+ channels, we examined whether key enzymes involved in the neurosteroidergic pathway are expressed within the ophthalmic branch of the TG using an RT-PCR analysis. We found that all the enzymes involved in the synthesis of PS, DHEA, and DHEAS—such as P450scc, P450c17, and

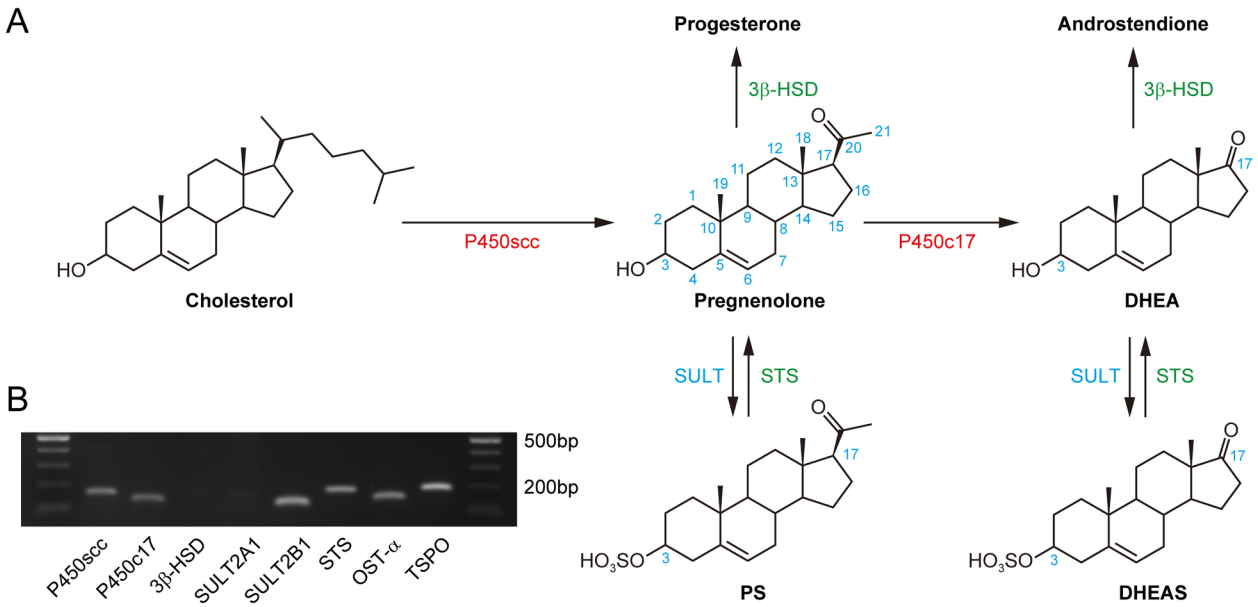

Fig. 1 Expression of enzymes involved in the biosynthesis of neurosteroids in the trigeminal ganglia. **A**, Neurosteroidogenic pathway illustrating the biosynthesis of pregnenolone, pregnenolone sulfate (PS), dehydroepiandrosterone (DHEA), and DHEA sulfate (DHEAS). P450scc, cytochrome P450 side-chain cleavage; SULT, sulfotransferase; STS, steroid sulfatase; P450c17, steroid 17α-hydroxylase; 3β-HSD, 3β-hydroxysteroid dehydrogenase. **B**, Expression of enzymes involved in the biosynthesis and membrane transport of PS. Total RNA was extracted from the ophthalmic branch of the trigeminal ganglion, and RT-PCR was performed. Transcripts for P450scc, P450c17, SULT2B1, and STS were clearly detected, whereas those for 3β-hydroxysteroid dehydrogenase and SULT2A1 were not detected. Transcripts for organic solute transporter-α (OST-α), a subunit involved in the transport of hydrophilic sulfated neurosteroids across the plasma membrane, and translocator protein (18 kDa; TSPO), which is involved in the translocation of cholesterol from the plasma membrane into mitochondria, were also detected in the ophthalmic branch of the trigeminal ganglion

SULT2B1—were detected in the ophthalmic region of the TG, except for 3β-HSD and SULT2A1 (Fig. 1B). Transcripts for 3β-HSD and SULT2A1 were clearly detected in the adrenal gland and liver, respectively (Fig. S1). The transcript for steroid sulfatase (STS), which hydrolyzes PS and DHEAS to pregnenolone and DHEA, respectively, was also detected (Fig. 1B). These results suggest that PS, DHEA, and DHEAS can be locally synthesized within the ophthalmic branch of the TG. Additionally, both the translocator protein (18 kDa), which is involved in the translocation of cholesterol from the plasma membrane into mitochondria [33], and organic solute transporter-α, a subunit involved in the transport of hydrophilic sulfated neurosteroids across the plasma membrane [34], were detected in the ophthalmic branch of TG (Fig. 1B).

Effect of PS on TTX-R I_{Na} in dural afferent neurons

In small-sized DiI-positive neurons (20–30 μm in diameter; Fig. S2A), the $Na_V1.8$-mediated TTX-R I_{Na} was recorded at a holding potential of −80 mV using voltage step stimulation (up to −10 mV, 100 ms duration, every 5 s) in the presence of both 300 nM TTX and 100 μM Cd^{2+} (Fig. S2B). To ensure complete rundown of the $Na_V1.9$-mediated current, all recordings were made at least 5 min after establishing whole-cell configuration using the F^--based internal solution [35]. In 33 of 35 small-sized DiI-positive neurons exhibiting TTX-R I_{Na}, capsaicin (500 nM), a transient receptor potential vanilloid 1 (TRPV1) agonist, induced an inward current (943.9 ± 101.2 pA, $n = 33$; Fig. S2C). As TRPV1 is considered as a representative marker for C-type neurons [36], most of the small-sized DiI-positive neurons used in the present study belong to C-type nociceptive neurons, as shown in our previous study [30].

Under these conditions, we examined the effects of various neurosteroids on the transient and persistent components of TTX-R I_{Na} (I_{NaT} and I_{NaP}, respectively; Fig. 2A). The most effective neurosteroids altering the TTX-R I_{Na} were PS and DHEA, where PS (100 μM) significantly increased the amplitudes of TTX-R I_{NaT} and I_{NaP} (I_{NaT}: 112.5 ± 3.0% of the control, $n = 8$, $p < 0.01$, and I_{NaP}: 129.4 ± 4.3% of the control, $n = 8$, $p < 0.01$; Fig. 2B, C). The effect of PS on TTX-R I_{NaT} and I_{NaP} was concentration-dependent; even at a concentration of 10 μM, PS significantly increased the amplitudes of TTX-R I_{NaT} and I_{NaP} (I_{NaT}: 102.2 ± 0.8% of the control, $n = 8$, $p < 0.01$; and I_{NaP}: 105.2 ± 1.4% of the control, $n = 8$, $p < 0.01$; Fig. 2D). The decay phase of TTX-R

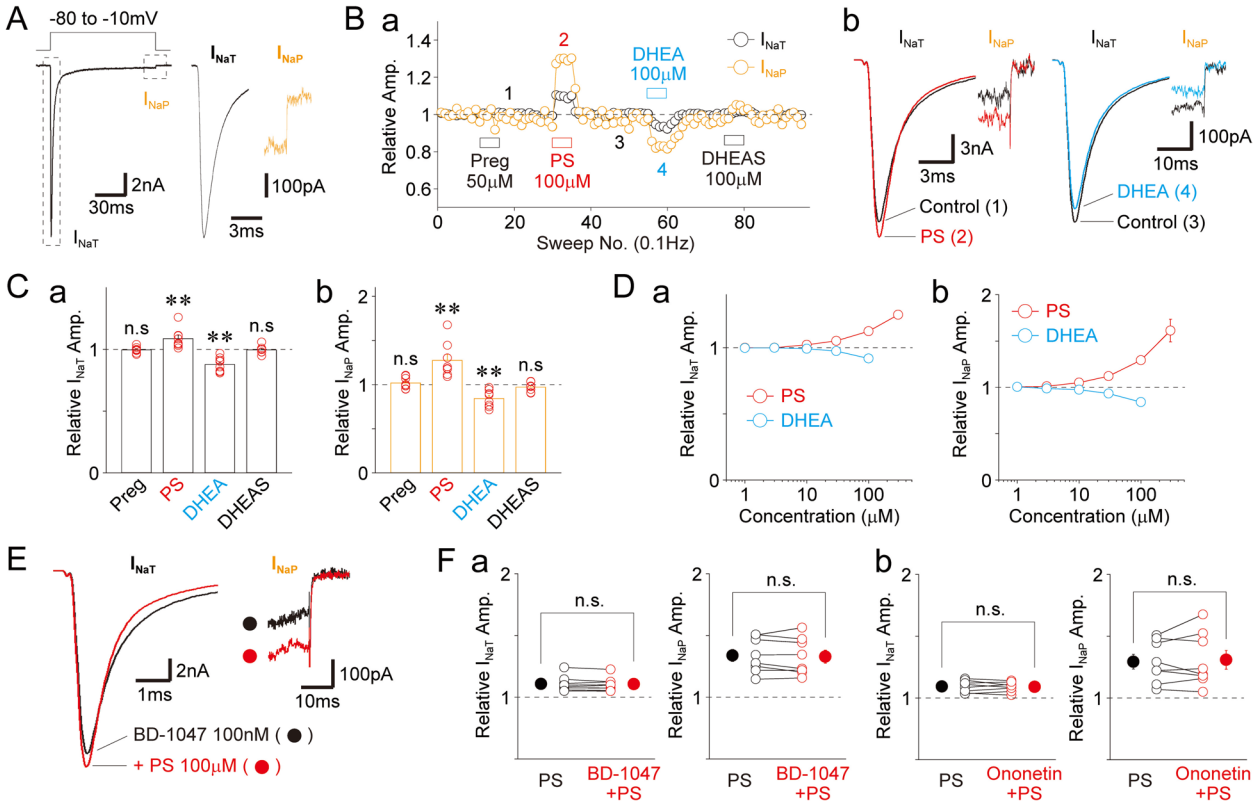

Fig. 2 Effects of neurosteroids on TTX-R I_{Na} in small-sized DiI-positive neurons. **A**, A typical TTX-R I_{Na} elicited by depolarizing step pulses (up to − 10 mV, 100 ms duration) at a holding potential of − 80 mV in the presence of 300 nM TTX and 100 μM Cd^{2+}. Insets show transient (I_{NaT}) and persistent (I_{NaP}) components of TTX-R I_{Na} with expanded time and amplitude scales. **B**, **a**, A typical time course of the relative amplitude of TTX-R I_{NaT} (black) and I_{NaP} (vermillion) recorded before, during, and after the application of pregnenolone (Preg; 50 μM), PS (100 μM), DHEA (100 μM), and DHEAS (100 μM). Each point was normalized to the amplitude of the first 10 recordings of TTX-R I_{NaT} or I_{NaP}. **b**, Representative traces of TTX-R I_{NaT} and I_{NaP} in the absence and presence of PS (left) and DHEA (right) at the numbered regions shown in *Ba*. **C**, Neurosteroid-induced changes in the amplitude of TTX-R I_{NaT} (**a**) and I_{NaP} (**b**). Open circles represent the individual results [pregnenolone (50 μM), $n = 8$; PS (100 μM), $n = 8$; DHEA (100 μM), $n = 8$; DHEAS (100 μM), $n = 8$], whereas columns and error bars indicate the mean and SEM. $^{**}p < 0.01$; n.s., not significant (paired t-test). **D**, Concentration–response relationships of PS and DHEA against TTX-R I_{NaT} (**a**) and I_{NaP} (**b**). Each point and error bar reflect the mean and SEM from eight (PS) and seven (DHEA) neurons. **E**, Typical TTX-R I_{NaT} and I_{NaP} obtained before and after the application of 100 μM PS in the presence of 100 nM BD-1047, a selective σ1 receptor antagonist. **F**, Changes induced by 100 μM PS in the amplitude of TTX-R I_{NaT} (left) and I_{NaP} (right) in the absence and presence of 100 nM BD-1047 (**a**) or 10 μM ononetin, a TRPM3 antagonist (**b**). Open circles connected by lines represent the individual results ($n = 8$), whereas closed circles and error bars indicate the mean and SEM. n.s., not significant (paired t-test)

I_{Na} was well fitted to a triple exponential function. We examined the resultant three kinetic parameters—fast (τ_{fast}), intermediate ($\tau_{intermediate}$), and slow (τ_{slow}) time constants—obtained in the absence and presence of 100 μM PS. While PS decreased the τ_{fast} value to 89.0 ± 2.4% of the control (1.1 ± 0.1 ms for the control and 0.9 ± 0.1 ms for PS, $n = 10$, $p < 0.05$), it increased the τ_{slow} value to 130.5 ± 7.6% of the control (25.8 ± 1.8 ms for the control and 32.7 ± 1.5 ms for PS, $n = 10$, $p < 0.01$; Fig. S2A, B). The weighted time constant ($\tau_{weighted}$) of TTX-R I_{Na} was decreased to 81.4% ± 2.2% of the control ($n = 10$, $p < 0.01$) in the presence of PS (Fig. S2A, B). The effect of PS on TTX-R I_{NaT} and I_{NaP} was not affected by adding either BD-1047 (100 nM), a selective σ1 receptor antagonist ($IC_{50} = 0.9$ nM; [37]), or ononetin (10 μM), a selective TRPM3 antagonist ($IC_{50} = 0.3$ μM; [38]) (Fig. 2E, F), suggesting that both σ1 receptor and TRPM3 are not involved in the PS-potentiation of TTX-R I_{Na}.

Conversely, while pregnenolone (50 μM) and DHEAS (100 μM) had no notable effect on either TTX-R I_{NaT} or I_{NaP}, DHEA (100 μM) significantly decreased the amplitudes of TTX-R I_{NaT} and I_{NaP} (I_{NaT}: 91.9 ± 2.3% of the control, $n = 7$, $p < 0.01$; and I_{NaP}: 84.2 ± 2.3% of the control, $n = 7$, $p < 0.01$; Fig. 2B, C). DHEA (100 μM) had no significant effect on the decay time constants of TTX-R I_{NaT} (Fig. S1C, D). The inhibitory effect of DHEA on TTX-R I_{NaT} and I_{NaP} was also concentration-dependent

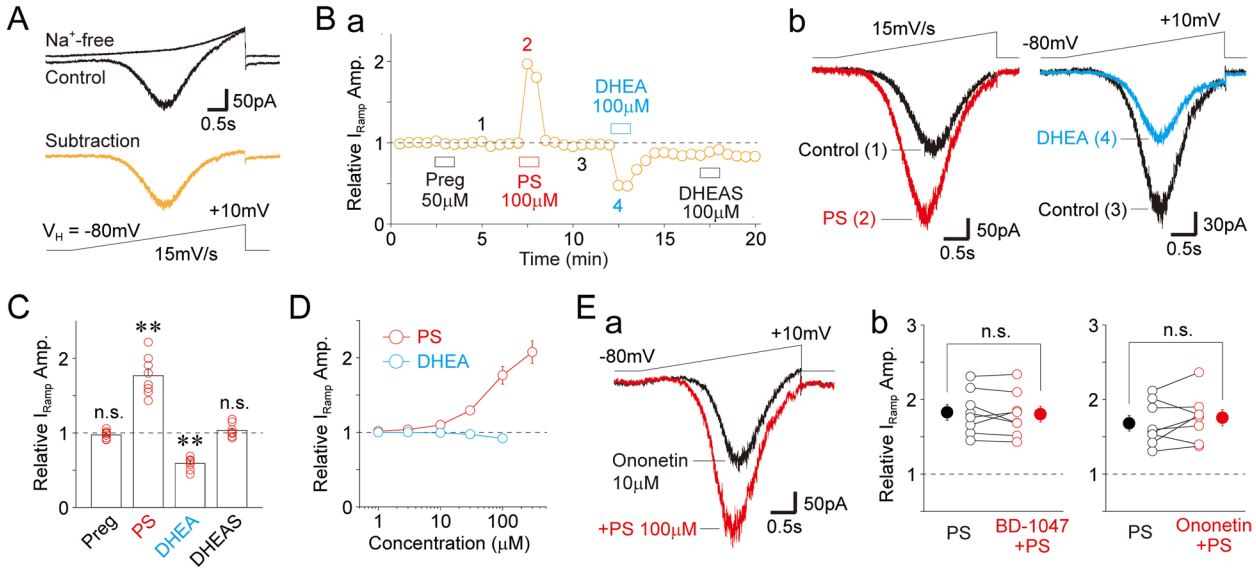

Fig. 3 Effects of neurosteroids on slow voltage-ramp-induced TTX-R I_{Na}. **A**, Typical raw traces of TTX-R I_{Ramp} elicited by slow voltage-ramp stimulation (−80 mV to +10 mV at 15 mV/s, every 20 s) in the absence (Na^+-free) and presence of extracellular Na^+. Subtracting the two traces yielded TTX-R I_{Ramp} (lower panel). **B**, **a**, A typical time course of the relative amplitude of TTX-R I_{Ramp} recorded before, during, and after the application of pregnenolone (Preg; 50 μM), PS (100 μM), DHEA (100 μM), and DHEAS (100 μM). Each point was normalized to the amplitude of the first five recordings of TTX-R I_{Ramp}. **b**, Representative traces of TTX-R I_{Ramp} in the absence and presence of PS (left) and DHEA (right) at the numbered regions shown in ***Ba.*** **C**, Neurosteroid-induced changes in the amplitude of TTX-R I_{Ramp}. Open circles represent the individual results [pregnenolone (50 μM), $n=8$; PS (100 μM), $n=8$; DHEA (100 μM), $n=8$; DHEAS (100 μM), $n=8$], whereas columns and error bars indicate the mean and SEM. $^{**}p<0.01$; n.s., not significant (paired t-test). **D**, Concentration–response relationships of PS and DHEA against TTX-R I_{Ramp}. Each point and error bar reflect the mean and SEM from eight (PS) and seven (DHEA) neurons. **E**, **a**, Typical TTX-R I_{Ramp} obtained before and after the application of 100 μM PS in the presence of 10 μM ononetin, a TRPM3 antagonist. **b**, Changes induced by 100 μM PS in the amplitude of TTX-R I_{Ramp} in the absence and presence of 100 nM BD-1047 (left) or 10 μM ononetin (right). Open circles connected by lines represent individual results ($n=8$), whereas closed circles and error bars indicate the mean and SEM. n.s., not significant (paired t-test)

(Fig. 2D) and was not affected by either BD-1047 (100 nM) or ononetin (10 μM) (Fig. S3A, B).

Since the I_{NaP} can also be elicited by slow voltage-ramp stimuli [39, 40], we examined the effects of neurosteroids on slow voltage-ramp–induced currents (I_{Ramp}) (−80 mV to +10 mV, 6 s duration, every 20 s) in small-sized DiI-positive neurons (Fig. 3A). As with the effects on TTX-R I_{NaP} shown in Fig. 2B, PS and DHEA had opposite effects on TTX-R I_{Ramp} (100 μM PS: 176.5 ± 11.8% of the control, $n=8$, $p<0.01$; and 100 μM DHEA: 57.2 ± 4.9% of the control, $n=7$, $p<0.01$; Fig. 3B, C). However, neither pregnenolone (50 μM) nor DHEAS (100 μM) altered the TTX-R I_{Ramp} (Fig. 3C). Even at a concentration of 10 μM, PS significantly increased the amplitudes of TTX-R I_{Ramp} (109.9 ± 1.4% of the control, $n=8$, $p<0.01$; Fig. 3D). The modulation of TTX-R I_{Ramp} by PS or DHEA was concentration-dependent (Fig. 3D). The effects of PS and DHEA on TTX-R I_{Ramp} were not affected by either BD-1047 (1 μM) or ononetin (10 μM) (Fig. 3E, Fig. S3C).

The PS-induced potentiation of TTX-R I_{NaT}, I_{NaP}, and I_{Ramp} was not affected by adding 100 μM intracellular PS (Fig. S4A, B), suggesting that PS acts extracellularly to potentiate TTX-R I_{Na}. We also examined whether endogenous PS modulates TTX-R I_{Na} in small-sized DiI-positive neurons by evaluating the effect of γ-CD, which is known to trap several kinds of neurosteroids, including PS [41]. Application of γ-CD (500 μM) alone had no effect on the basal amplitudes of TTX-R I_{NaT}, I_{NaP}, and I_{Ramp} (Fig. S4C, D), suggesting that the role of endogenous PS in the basal modulation of TTX-R Na^+ channels may be negligible under the present experimental conditions, such as in isolated single neurons.

In another set of experiments, we examined whether PS and DHEA affect the current mediated by $Na_V1.9$, another TTX-R Na^+ channel subtype expressed in nociceptive sensory neurons [17]. The $Na_V1.9$-mediated current was recorded by depolarizing step pulses from a holding potential of − 120 mV (Fig. S5A). PS also significantly increased the amplitude of the $Na_V1.9$-mediated current in a concentration-dependent manner (Fig. S5B–D). In contrast, DHEA potently decreased the amplitude of the $Na_V1.9$-mediated current, with an IC_{50} value of 49.2 μM (Fig. S5B–D).

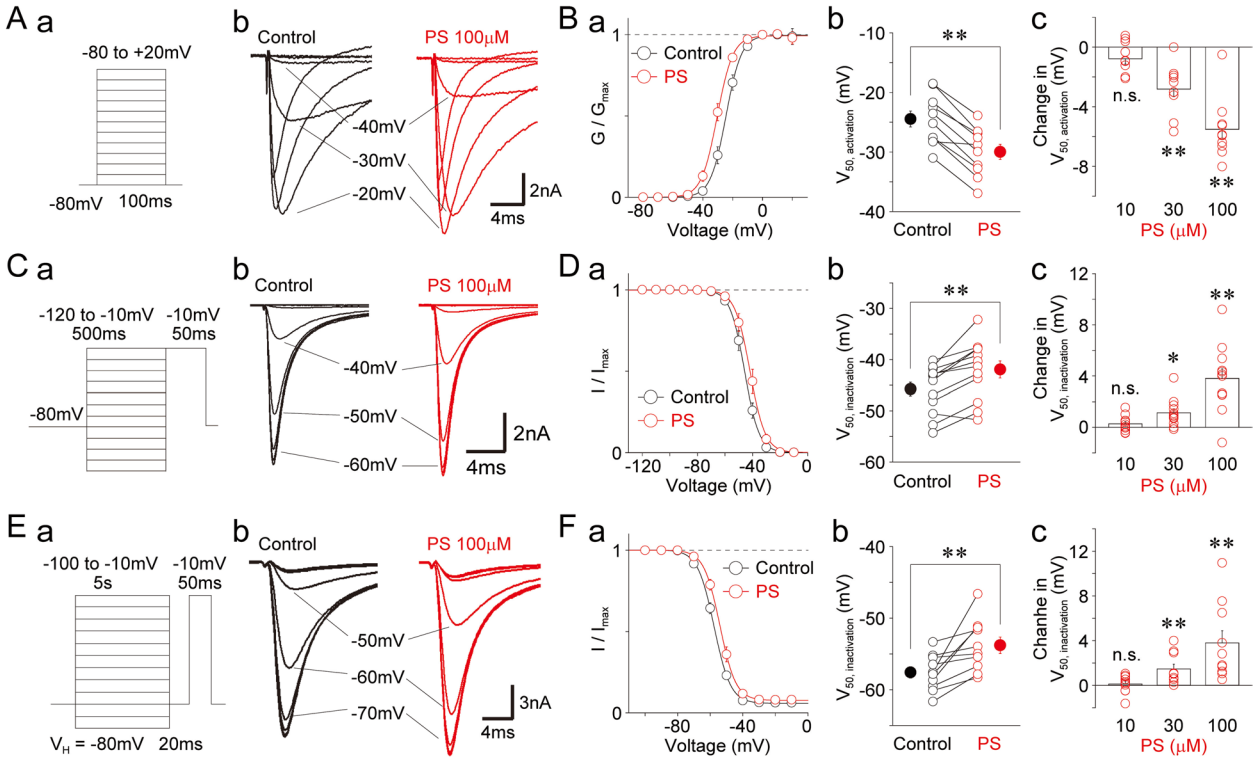

Fig. 4 Effect of PS on the voltage dependence of TTX-R Na^+ channels. **A**, **a**, Schematic illustration of voltage step pulses used to assess the voltage-activation relationship of TTX-R Na^+ channels. TTX-R I_{Na} was induced by 100 ms depolarizing pulses in 10 mV increments from a holding potential of − 80 mV. **b**, Representative raw traces of TTX-R I_{Na} elicited by voltage step pulses in the absence (left) and presence (right) of 100 μM PS. **B**, **a**, Voltage-activation relationships of TTX-R Na^+ channels in the absence (black circles) and presence (red circles) of 100 μM PS. Continuous lines represent the best fits to the Boltzmann function. Each point and error bar represent the mean and SEM from 10 neurons. **b**, Changes induced by 100 μM PS in the midpoint voltage for activation ($V_{50,\ activation}$) of TTX-R Na^+ channels. Open circles connected by lines represent the individual results ($n = 10$), while closed circles and error bars indicate the mean and SEM. $^{**}p < 0.01$ (paired t-test). **c**, Concentration-response relationship of PS on $V_{50,\ activation}$. Open circles represent the individual results ($n = 10$ for each concentration); columns and error bars indicate the mean and SEM. $^{**}p < 0.01$; n.s., not significant (paired t-test). **C**, **a**, Schematic illustration of voltage step pulses used to assess the steady-state fast inactivation of TTX-R Na^+ channels. TTX-R I_{Na} was induced by 50 ms depolarizing pulses from − 120 to − 10 mV in 10 mV increments from a holding potential of − 80 mV. **b**, Representative raw traces of TTX-R I_{Na} elicited by voltage step pulses in the absence (left) and presence (right) of 100 μM PS. **D**, **a**, Steady-state fast inactivation relationships of TTX-R Na^+ channels in the absence (black circles) and presence (red circles) of 100 μM PS. Continuous lines represent the best fits to the Boltzmann function. Each point and error bar represent the mean and SEM from 12 neurons. **b**, Changes induced by 100 μM PS in the midpoint voltage for inactivation ($V_{50,\ inactivation}$) of TTX-R Na^+ channels. Open circles connected by lines represent the individual results ($n = 12$); closed circles and error bars indicate the mean and SEM. $^{**}p < 0.01$ (paired t-test). **c**, Concentration-response relationship of PS on $V_{50,\ inactivation}$. Open circles represent the individual results ($n = 12$ for each concentration); columns and error bars indicate the mean and SEM. $^{**}p < 0.01$; n.s., not significant (paired t-test). **E**, **a**, Schematic illustration of voltage step pulses used to assess slow inactivation of TTX-R Na^+ channels. Conditioning prepulses (5 s duration) from − 100 mV to − 10 mV in 10 mV increments were followed by test pulses (50 ms duration) to − 10 mV, with an interval of 20 ms, from a holding potential of − 80 mV. **b**, Representative raw traces of TTX-R I_{Na} elicited by voltage step pulses in the absence (left) and presence (right) of 100 μM PS. **F**, **a**, Voltage dependence of slow inactivation of TTX-R Na^+ channels in the absence (black circles) and presence (red circles) of 100 μM PS. Continuous lines represent the best fits to the Boltzmann function. Each point and error bar represent the mean and SEM from 10 neurons. **b**, Changes induced by 100 μM PS in the midpoint voltage for slow inactivation ($V_{50,inactivation}$) of TTX-R Na^+ channels. Open circles connected by lines represent individual results ($n = 10$); closed circles and error bars indicate the mean and SEM. $^{**}p < 0.01$ (paired t-test). **c**, Concentration–response relationship of PS on $V_{50,inactivation}$. Open circles represent individual results ($n = 10$ for each concentration); columns and error bars indicate the mean and SEM. $^{**}p < 0.01$; n.s., not significant (paired t-test)

Effect of PS on voltage-dependence of TTX-R Na^+ channels in dural afferent neurons

To investigate the effect of PS on the voltage-activation relationship of TTX-R Na^+ channels, TTX-R I_{Na} was elicited by depolarizing test pulses (100 ms duration, up to + 20 mV in 10 mV increments; Fig. 4A). Conductances in the absence and presence of PS were then calculated and fitted to the Boltzmann function (Fig. 4Ba). PS shifted the midpoint voltage for activation ($V_{50,activation}$) toward a hyperpolarized range in a dose-dependent manner. At a concentration of 100 μM, PS shifted the $V_{50,activation}$ value by − 5.5 ± 0.6 mV (from − 24.5 ± 1.3 mV for the control

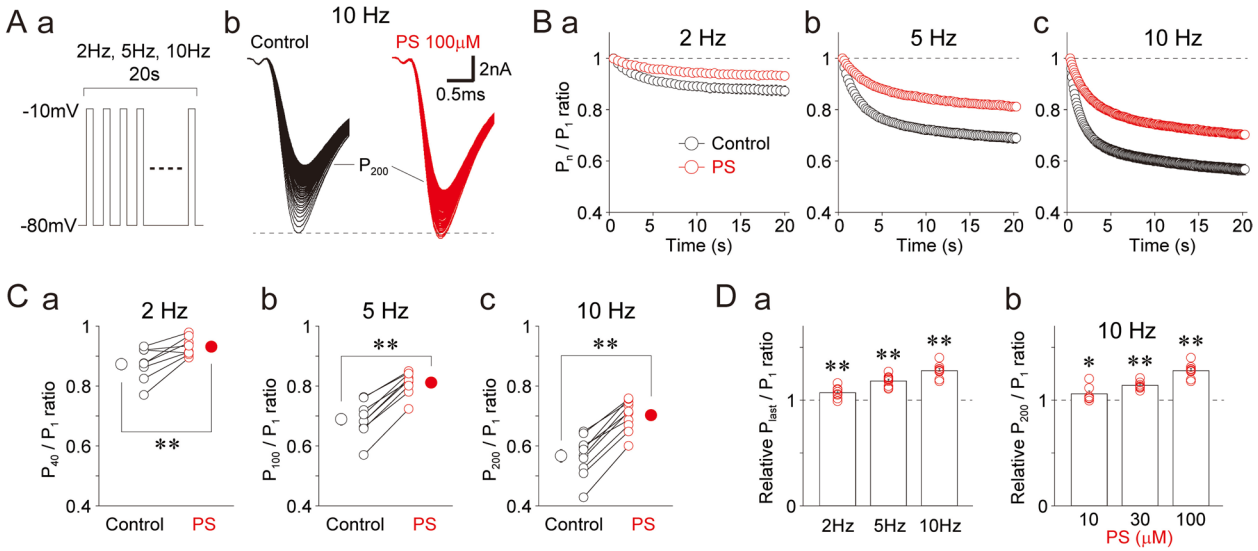

Fig. 5 Effect of PS on the use-dependent inhibition of TTX-R Na^+ channels. **A**, **a**, Schematic illustration of voltage step pulses used to assess the use-dependent inhibition of TTX-R Na^+ channels. TTX-R I_{Na} was elicited by successive voltage step pulses from −80 mV to −10 mV (10 ms duration) for 20 s at frequencies of 2 Hz (40 pulses), 5 Hz (100 pulses), and 10 Hz (200 pulses). **b**, Representative raw traces of TTX-R I_{Na} elicited by voltage step pulses at 10 Hz in the absence (left) and presence (right) of 100 μM PS. **B**, Time courses of the peak amplitude of TTX-R I_{Na} during trains of pulses at 2 Hz (40 pulses, **a**), 5 Hz (100 pulses, **b**), and 10 Hz (200 pulses, **c**), in the absence (black circles) and presence (red circles) of 100 μM PS. The peak amplitudes of all TTX-R I_{Na} (P_n) were normalized to that of the first pulse (P_1). Each point and error bar represent the mean and SEM from 8 (2 Hz), 9 (5 Hz), and 10 (10 Hz) neurons. **C**, Changes induced by 100 μM PS in the ratio of the last peak amplitude (P_{40}, P_{100}, or P_{200}) to the first (P_1) for 2 Hz (**a**), 5 Hz (**b**), and 10 Hz (**c**). Open circles connected by lines represent individual results ($n = 8$ for 2 Hz, $n = 9$ for 5 Hz, $n = 10$ for 10 Hz); closed circles and error bars indicate the mean and SEM. $^{**}p < 0.01$ (paired t-test). **D**, **a**, Changes induced by 100 μM PS in the P_{last}/P_1 ratios for different frequencies. Open circles represent individual results ($n = 8$ for 2 Hz, $n = 9$ for 5 Hz, $n = 10$ for 10 Hz); columns and error bars indicate the mean and SEM. $^{**}p < 0.01$ (paired t-test). **b**, Concentration–response relationships of PS on the use-dependent inhibition at 10 Hz. Open circles represent individual results ($n = 7$ for 10 μM, $n = 7$ for 30 μM, $n = 10$ for 100 μM); columns and error bars indicate the mean and SEM. $^{*}p < 0.05$; $^{**}p < 0.01$ (paired t-test)

to −30.0 ± 1.3 mV with PS, $n = 10$, $p < 0.01$; Fig. 4B). The slope factor k was not affected by PS (4.8 ± 0.3 for the control and 5.0 ± 0.2 for the PS condition, $n = 10$, $p = 0.36$).

Next, to assess the effect of PS on the steady-state fast inactivation relationship of TTX-R Na^+ channels, the TTX-R I_{Na} was elicited by depolarizing test pulses (100 ms duration, up to −10 mV) after 500 ms prepulses from −120 mV to −10 mV in 10 mV increments (Fig. 4C). The normalized TTX-R I_{Na} in the absence and presence of PS was calculated and fitted to the Boltzmann function (Fig. 4Da). PS shifted the midpoint voltage for inactivation ($V_{50,inactivation}$) toward a depolarized range in a dose-dependent manner. At 100 μM, PS shifted the $V_{50,inactivation}$ value by +3.8 ± 0.7 mV (from −45.7 ± 1.4 mV for the control to −41.9 ± 1.7 mV with PS, $n = 12$, $p < 0.01$; Fig. 4D). The slope factor k was unaffected by PS (4.4 ± 0.1 for the control and 4.3 ± 0.1 for the PS condition, $n = 12$, $p = 0.24$).

We also examined whether PS affects the voltage dependence of slow inactivation of TTX-R Na^+ channels. The TTX-R I_{Na} was elicited by depolarizing test pulses (100 ms duration, up to −10 mV) after 5 s prepulses from −100 mV to −10 mV in 10 mV increments, with a 20 ms interpulse interval (Fig. 4E). The normalized TTX-R I_{Na} recorded in the absence and presence of PS was calculated and fitted to the Boltzmann function (Fig. 4Fa). PS shifted the $V_{50,\ inactivation}$ toward a depolarized range in a dose-dependent manner. At a concentration of 100 μM, PS shifted the $V_{50,inactivation}$ value by +3.8 ± 1.1 mV (from −57.6 ± 0.8 mV for the control to −53.8 ± 1.1 mV with PS, $n = 10$, $p < 0.01$; Fig. 4Fb, c). In contrast to PS, DHEA had minor effects on the voltage dependence of TTX-R Na^+ channels (Fig. S6).

Effect of PS on the use-dependent inhibition of TTX-R Na^+ channels in dural afferent neurons

We examined the effect of PS on the use-dependent inhibition of TTX-R Na^+ channels. TTX-R I_{Na} was elicited by a 20 s series of 40 (2 Hz), 100 (5 Hz), and 200 (10 Hz) depolarizing test pulses (10 ms duration, up to −10 mV) in the absence and presence of 100 μM PS (Fig. 5A). Each TTX-R I_{Na} recorded in the absence and presence of 100 μM PS was normalized to the first TTX-R I_{Na} and plotted (Fig. 5B). PS (100 μM) significantly increased the amplitude ratio of the last TTX-R I_{Na} (P_{40}, P_{100}, and P_{200} for 2 Hz, 5 Hz, and 10 Hz, respectively) relative to the

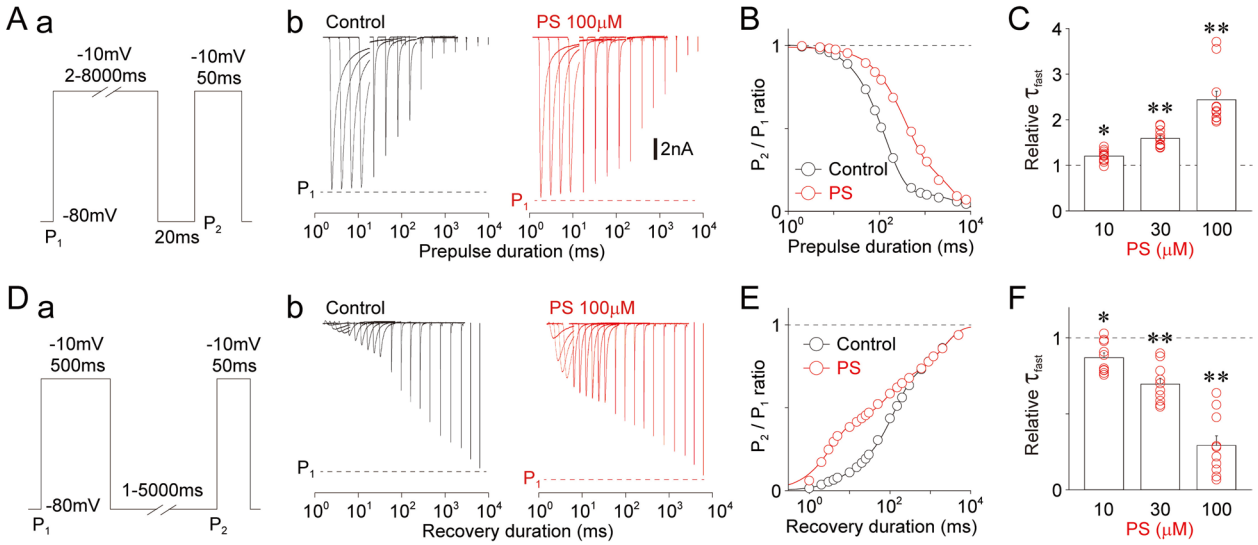

Fig. 6 Effect of PS on the inactivation and recovery kinetics of TTX-R Na^+ channels. **A**, **a**, Schematic illustration of voltage step pulses used to study the development of inactivation of TTX-R Na^+ channels. TTX-R I_{Na} was induced using a two-pulse protocol, where the first conditioning pulses (P_1; depolarization to − 10 mV, 2–8000 ms duration) were followed by second test pulses (P_2; depolarization to − 10 mV, 50 ms duration). The second TTX-R I_{Na} was recorded after an interpulse interval of 20 ms at a holding potential of − 80 mV. **b**, Representative raw traces of the second TTX-R I_{Na} (P_2) elicited by voltage step pulses in the absence (left) and presence (right) of 100 μM PS. Dotted lines represent the first TTX-R I_{Na} (P_1). **B**, Kinetics of the development of TTX-R Na^+ channel inactivation in the absence (black circles) and presence (red circles) of 100 μM PS. The P_2/P_1 ratio was plotted against the duration of the prepulse. Continuous lines represent the best fit to a double exponential function. Each point and error bar represent the mean and SEM from 11 neurons. **C**, Concentration–response relationship of PS on the fast time constant (τ_{fast}) of inactivation kinetics. Open circles represent individual results ($n = 11$ for each concentration); columns and error bars indicate the mean and SEM. $^*p < 0.05$; $^{**}p < 0.01$ (paired t-test). **D**, **a**, Schematic illustration of voltage step pulses used to study recovery from TTX-R Na^+ channel inactivation. TTX-R I_{Na} was induced using a two-pulse protocol, where the first conditioning pulses (P_1; depolarization to − 10 mV, 500 ms duration) were followed by second test pulses (P_2; depolarization to − 10 mV, 50 ms duration). The second TTX-R I_{Na} was recorded after interpulse intervals ranging from 1 to 5000 ms at a holding potential of − 80 mV. **b**, Representative raw traces of the second TTX-R I_{Na} (P_2) elicited by voltage step pulses in the absence (left) and presence (right) of 100 μM PS. Dotted lines represent the first TTX-R I_{Na} (P_1). **E**, Kinetics of recovery from TTX-R Na^+ channel inactivation in the absence (black circles) and presence (red circles) of 100 μM PS. The P_2/P_1 ratio was plotted against the recovery time. Continuous lines represent the best fit to a triple exponential function. Each point and error bar represent the mean and SEM from 10 neurons. **F**, Concentration–response relationship of PS on the fast time constant (τ_{fast}) of recovery kinetics. Open circles represent individual results ($n = 10$ for each concentration); columns and error bars indicate the mean and SEM. $^*p < 0.05$; $^{**}p < 0.01$ (paired t-test)

first TTX-R I_{Na} (P_1). Specifically, PS increased the P_{200}/P_1 ratio to 127.9 ± 1.9% of the control (from 0.57 ± 0.02 for the control to 0.70 ± 0.02 with PS, $n = 10$, $p < 0.01$; Fig. 5C, Da). PS (100 μM) also increased the P_{40}/P_1 and P_{100}/P_1 ratios (to 107.0% ± 1.9% for the P_{40}/P_1, $n = 8$, $p < 0.01$, and 118.1% ± 1.8% for the P_{100}/P_1, $n = 9$, $p < 0.01$; Fig. 5C, Da). Additionally, the PS-induced potentiation of the P_{200}/P_1 ratio was concentration-dependent (Fig. 5Db). In contrast, DHEA had no effect on the use-dependent inhibition of TTX-R Na^+ channels (Fig. S7).

Effect of PS on inactivation and recovery kinetics of TTX-R Na^+ channels in dural afferent neurons

We investigated the effect of PS on the onset of inactivation of TTX-R Na^+ channels. TTX-R I_{Na} was elicited using a two-pulse protocol, where the first conditioning pulse (P_1; 2–8000 ms duration, up to − 10 mV) was followed by a second test pulse (P_2; 50 ms duration, up to − 10 mV) with a 20 ms interpulse interval, in the absence and presence of 100 μM PS (Fig. 6A). The amplitude ratio of the two TTX-R I_{Na} (P_2/P_1) was plotted against the duration of the first pulse, and the P_2/P_1 ratios observed in the absence and presence of PS were fitted to a double exponential function (Fig. 6B), yielding two kinetic parameters: fast (τ_{fast}) and slow (τ_{slow}) time constants. PS significantly delayed the onset of inactivation in a concentration-dependent manner (Fig. 6C). At 100 μM, PS increased the τ_{fast} value to 243.9 ± 18.6% of the control (from 140.1 ± 10.9 ms for the control to 345.0 ± 38.8 ms with PS, $n = 11$, $p < 0.01$; Fig. 6C, Fig. S8Aa). PS (100 μM) also affected other kinetic parameters, such as τ_{slow}, A_{fast}, and A_{slow} values (Fig. S8A). In contrast, DHEA at 100 μM slightly but significantly decreased the τ_{fast} value for the development of inactivation (Fig. S9A–D).

Next, we examined the effect of PS on the recovery from inactivation of TTX-R Na^+ channels. TTX-R I_{Na} was elicited using a two-pulse protocol, where the first conditioning pulse (P_1; 500 ms duration, up to − 10 mV)

was followed by a second test pulse (P_2; 50 ms duration, up to −10 mV) with interpulse intervals of 1–5000 ms, in the absence and presence of 100 μM PS (Fig. 6D). The P_2/P_1 ratios observed in the absence and presence of PS were plotted against the recovery time and fitted to a triple exponential function (Fig. 6E), yielding three kinetic parameters: fast (τ_{fast}), intermediate ($\tau_{intermediate}$), and slow (τ_{slow}) time constants. PS significantly accelerated the recovery from inactivation of TTX-R Na^+ channels in a concentration-dependent manner (Fig. 6F). At 100 μM, PS decreased the τ_{fast} value to 29.2 ± 6.3% of the control (from 17.9 ± 3.4 ms for the control to 3.6 ± 0.3 ms with PS, $n = 10$, $p < 0.01$; Fig. 6F, Fig. S8Ba). PS (100 μM) also affected the $\tau_{intermediate}$, A_{fast}, and $A_{intermediate}$ values without affecting the τ_{slow} and A_{slow} values (Fig. S8B). In contrast, DHEA at 100 μM slightly but significantly increased the τ_{fast} value of recovery from inactivation (Fig. S9E–H).

Effect of PS on the excitability of dural afferent neurons

First, we examined whether PS affects the basal excitability of dural afferent neurons under current-clamp conditions. All subsequent current-clamp experiments were conducted in the presence of 300 nM TTX to examine the effect of PS on TTX-R Na^+ channels in nociceptive neurons. In the majority of small-sized DiI-positive neurons tested (42 of 45 neurons, 93%), PS caused a concentration-dependent hyperpolarization of the membrane potential (for 100 μM PS, −5.3 ± 0.7 mV, $n = 11$, $p < 0.01$; Fig. 7A). In voltage-clamp recordings, PS (100 μM) induced an outward membrane current at a holding potential of −20 mV in the same DiI-positive neurons (71.3 ± 7.2 pA, $n = 8$; Fig. 7B). This outward current was accompanied by a decrease in input resistance (to 75.9% ± 2.3% of the control, $n = 8$, $p < 0.01$; Fig. 7B), indicating that PS increased ionic conductance. The reversal potential of the PS-induced current was similar to the equilibrium potential of K^+ (Fig. S10A). The PS-induced current was not affected by adding 100 nM BD-1047 (Fig. S10B), consistent with the lack of involvement of the G-protein-coupled σ1 receptor in the PS-induced membrane current. The PS-induced current was greatly decreased in the presence of either acidic extracellular solution (pH 6.0) or A-1899 (1 μM), a TASK-1/TASK-3 inhibitor [42] (Fig. S10C, D). Taken together, these results suggest that the PS-induced membrane hyperpolarization is likely due to increased leak K^+ conductance through acid-sensitive two-pore domain K^+ (K2P) channel subtypes.

Under current-clamp conditions, a subset of small-sized DiI-positive neurons (8 of 45 neurons, 18%) exhibited spontaneous action potentials at rest (Fig. 7C). In these neurons, PS (100 μM) increased the mean frequency of action potentials in a concentration-dependent manner (for 100 μM PS, 181.1% ± 13.6% of the control, $n = 8$, $p < 0.05$; Fig. 7D). The PS-induced increase in the frequency of spontaneous action potentials was prominent immediately after the application of PS (Fig. 7Cb′). In contrast, spontaneous action potentials were greatly reduced immediately after the washout of PS (Fig. 7Ac′), suggesting that PS had dual effects on spontaneous action potentials. Considering that I_{NaP} is known to regulate the generation of spontaneous action potentials in several brain regions [43–45], and given that PS increased the TTX-R I_{NaP} as shown above, the PS-induced potentiation of TTX-R I_{NaP} might be responsible for the observed increase in spontaneous action potential frequency. This was supported by the finding that riluzole (10 μM), a specific I_{NaP} inhibitor [46] (see also Fig. 8F), potently decreased the frequency of spontaneous action potentials with an IC_{50} value of 1.8 μM in small-sized DiI-positive neurons (Fig. 7E). PS (100 μM) did not generate any spontaneous action potentials in the presence of 10 μM riluzole (Fig. 7F). However, riluzole (10 μM) had a minor effect on TTX-R I_{Na} (96.4% ± 0.9% of the control, $n = 8$, $p < 0.01$; Fig. 7F inset). On the other hand, DHEA had no effect on the membrane potentials and the frequency of spontaneous action potentials (Fig. S11A).

Next, we examined whether PS affects the threshold for action potential generation. When depolarizing current stimuli were applied to small-sized DiI-positive neurons, PS decreased the rheobase current in a concentration-dependent manner (Fig. 8A, B). Although PS (100 μM) hyperpolarized these neurons (Fig. 8A), it decreased the rheobase current to 77.8% ± 3.8% of the control (139.1 ± 13.2 pA for the control and 110.9 ± 13.8 pA for PS, $n = 11$, $p < 0.01$; Fig. 8A, Ba). When hyperpolarizing current stimuli (DC; −40 to −50 pA) were injected into DiI-positive neurons, the membrane potential hyperpolarized by −5.0 ± 0.3 mV ($n = 6$), similar to the hyperpolarization induced by 100 μM PS. Unlike the PS effect on the rheobase current, the hyperpolarizing DC current increased the rheobase current to 112.6% ± 3.2% of the control (131.7 ± 13.0 pA for the control and 148.3 ± 15.6 pA for DC injection, $n = 6$, $p < 0.05$; Fig. 8Bc). This indicates that PS decreased the threshold for action potential generation independent of membrane hyperpolarization. In contrast, DHEA had no effect on the threshold for action potential generation (Fig. S11B, C).

We also examined whether PS affects the number of action potentials elicited by depolarizing current stimuli. When depolarizing current stimuli [multiples of the threshold (T) current (1T–4T)] were applied to small-sized DiI-positive neurons, we observed phasic (34 of 54 neurons tested), tonic (14 of 54 neurons tested), and single (6 of 54 neurons tested) firing patterns in response to 3T current stimuli. This proportion was largely similar to that reported in our previous study [30]. Data obtained

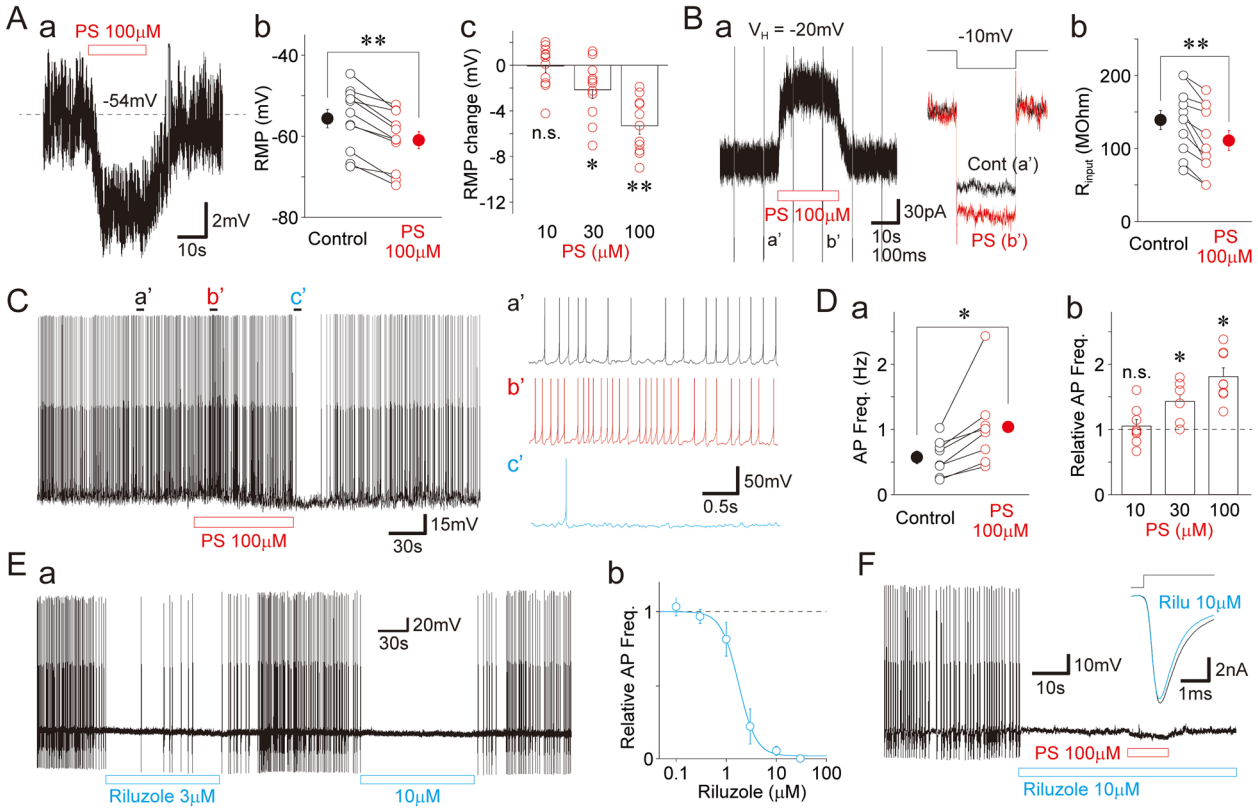

Fig. 7 Effect of PS on the basal excitability of small sized DiI-positive neurons.**A**, **a**, Typical raw trace recorded before, during, and after the application of 100 μM PS under current-clamp conditions. The resting membrane potential of this neuron was − 54 mV. **b**, Changes induced by 100 μM PS in resting membrane potential. Open circles represent individual results ($n = 11$); closed circles and error bars indicate the mean and standard error of the mean (SEM). $^{**}p < 0.01$ (paired t-test). **c**, Concentration–response relationship of PS on the membrane potentials of DiI-positive neurons. Open circles represent individual results ($n = 11$ for each concentration); columns and error bars indicate the mean and SEM. $^{*}p < 0.05$; $^{**}p < 0.01$; n.s., not significant (paired t-test). **B**, **a**, Typical raw trace recorded before, during, and after the application of 100 μM PS at a holding potential of − 20 mV under voltage-clamp conditions. Hyperpolarizing step pulses (− 10 mV, 300 ms duration) were applied to patched neurons every 10 s. Insets represent the current responses to hyperpolarizing step pulses in the absence (black trace, a') and presence (red trace, b') of 100 μM PS. **b**, Changes induced by 100 μM PS in input resistance (R_{input}). Open circles represent individual results ($n = 8$); closed circles and error bars indicate the mean and SEM. $^{**}p < 0.01$ (paired t-test). **C**, Typical raw trace exhibiting spontaneous action potentials recorded before, during, and after the application of 100 μM PS under current-clamp conditions. Note that spontaneous action potentials increased immediately after application (b') and decreased after washout (c') of 100 μM PS. **D**, **a**, Changes induced by 100 μM PS in action potential (AP) frequency. Open circles represent individual results ($n = 8$); closed circles and error bars indicate the mean and SEM. $^{*}p < 0.05$ (paired t-test). **b**, Concentration–response relationship of PS on AP frequency. Open circles represent individual results ($n = 8$ for each concentration); columns and error bars indicate the mean and SEM. $^{*}p < 0.05$; n.s., not significant (paired t-test). **E**, **a**, Typical raw trace exhibiting spontaneous action potentials recorded before, during, and after the application of riluzole (3 μM and 10 μM), a specific I_{NaP} inhibitor. **b**, Concentration–response relationship of riluzole on action potential frequency. A continuous line represents the best fit using least squares fitting; the IC_{50} was 1.8 μM. Each point and error bar indicate the mean and SEM from six neurons. **F**, Typical raw trace exhibiting spontaneous action potentials recorded before, during, and after the application of 100 μM PS in the presence of 10 μM riluzole. Inset shows typical raw traces of TTX-R I_{Na} elicited by depolarizing step pulses (up to − 10 mV, 100 ms duration) at a holding potential of − 80 mV in the absence (black) and presence (cyan) of 10 μM riluzole. Note that PS did not elicit any spontaneous action potentials in the presence of 10 μM riluzole

from small-sized DiI-positive neurons exhibiting the single firing pattern were not included in this analysis, as changes in the number of action potentials cannot be evaluated in these cells. Figure 8C shows typical action potentials in response to 1T–4T current stimuli in the absence and presence of 100 μM PS in small-sized DiI-positive neurons exhibiting the phasic firing pattern. PS significantly increased the number of action potentials elicited by depolarizing current stimuli in a concentration-dependent manner (Fig. 8Db). At a concentration of 100 μM, PS increased the number of action potentials elicited by 4T stimuli to 286.7% ± 53.9% of the control (4.6 ± 0.8 for the control and 11.3 ± 1.6 for PS, $n = 11$, $p < 0.01$; Fig. 8D). In contrast, DHEA at 100 μM slightly decreased the number of action potentials elicited by depolarizing current stimuli (Fig. S11D, E).

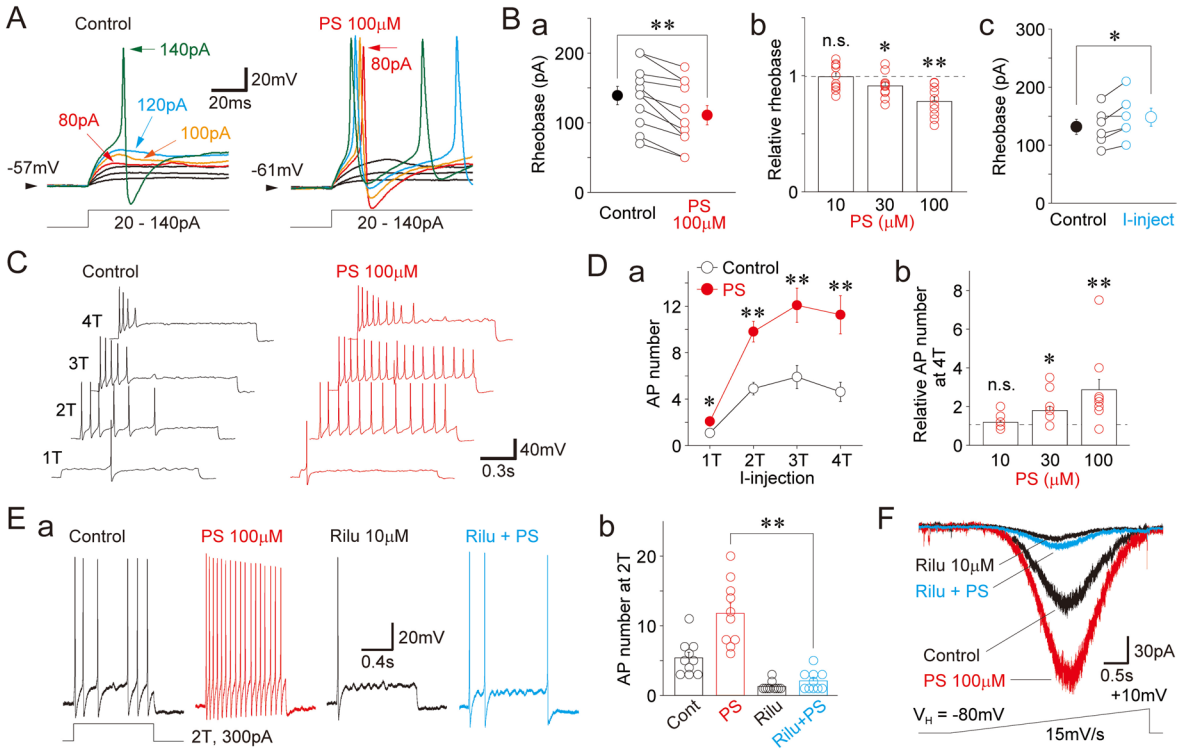

Fig. 8 Effect of PS on action potentials in response to depolarizing stimuli.**A**, Typical raw traces recorded in response to successive depolarizing current stimuli (20 pA increments, 500 ms duration) in the absence (left panel) and presence (right panel) of 100 μM PS. The rheobase current—the minimum current required to generate action potentials—was 140 pA without PS and 80 pA with 100 μM PS. **B**, **a**, Changes in rheobase current induced by 100 μM PS. Open circles represent individual results ($n = 11$); closed circles and error bars indicate the mean and SEM. $^{**}p < 0.01$ (paired t-test). **b**, Concentration–response relationship of PS on rheobase current. Open circles represent individual results ($n = 11$ for 10 μM, $n = 11$ for 30 μM, $n = 11$ for 100 μM); bars indicate the mean and SEM. $^{*}p < 0.05$; n.s., not significant (paired t-test). **c**, Changes in rheobase current induced by hyperpolarizing direct current (DC). In all neurons tested, hyperpolarizing DC caused membrane hyperpolarization by −4.1 mV to −5.9 mV (5.0 ± 0.3 mV, $n = 6$). Unlike PS, hyperpolarizing DC increased the rheobase current. Open circles represent individual results ($n = 6$); closed circles and error bars indicate the mean and SEM. $^{**}p < 0.01$ (paired t-test). **C**, Typical raw traces recorded in response to four successive depolarizing current stimuli at multiples of the threshold (T) current (1T–4T; 1T = 110 pA, 1 s duration) in the absence (left panel) and presence (right panel) of 100 μM PS. **D**, **a**, Changes in the number of action potentials elicited by depolarizing current stimuli induced by 100 μM PS. Each point and error bar represent the mean and SEM from 11 neurons. $^{*}p < 0.05$; $^{**}p < 0.01$ (paired t-test). **b**, Concentration–response relationship of PS on the number of action potentials elicited by depolarizing current stimuli (4T). Open circles represent individual results ($n = 11$ for each concentration); bars indicate the mean and SEM. $^{*}p < 0.05$; $^{**}p < 0.01$; n.s., not significant (paired t-test). **E**, **a**, Typical raw traces recorded in response to depolarizing current stimuli [2T (300 pA), 1 s duration] before and during the application of 100 μM PS, both in the absence and presence of 10 μM riluzole. **b**, Changes in the number of action potentials elicited by depolarizing current stimuli (2T) induced by 100 μM PS in the absence and presence of 10 μM riluzole. Each bar and error bar represent the mean and SEM from 10 neurons. $^{**}p < 0.01$ (paired t-test). **F**, Typical raw traces of TTX-R I_{Ramp} elicited by slow voltage-ramp stimulation (−80 mV to + 10 mV at 15 mV/s, every 20 s) before and during the application of 100 μM PS, both without and with 10 μM riluzole

Given that TTX-R I_{NaP} is directly involved in the repetitive generation of action potentials in dural afferent neurons [23], we further examined the effect of riluzole on the PS-induced increase in the number of action potentials. Application of riluzole (10 μM) greatly decreased the number of action potentials elicited by depolarizing current stimuli (2T) (Fig. 8E), indicating that the riluzole-sensitive TTX-R I_{NaP} is also involved in the generation of action potentials elicited by depolarizing stimuli (see also [23]). Riluzole (10 μM) also significantly reduced the PS-induced increase in the number of action potentials to 16.7% ± 1.7% of the PS condition (11.8 ± 1.5 for PS alone and 2.1 ± 0.4 for PS plus riluzole, $n = 10$, $p < 0.01$; Fig. 8E). In another set of experiments, we also found that riluzole greatly decreased the PS-induced increase in TTX-R I_{Ramp} in small-sized DiI-positive neurons (Fig. 8F).

Effect of PS on the shape of action potentials in dural afferent neurons

Finally, we examined whether PS affects the shape of single action potentials in small-sized DiI-positive neurons. Although PS (100 μM) hyperpolarized the

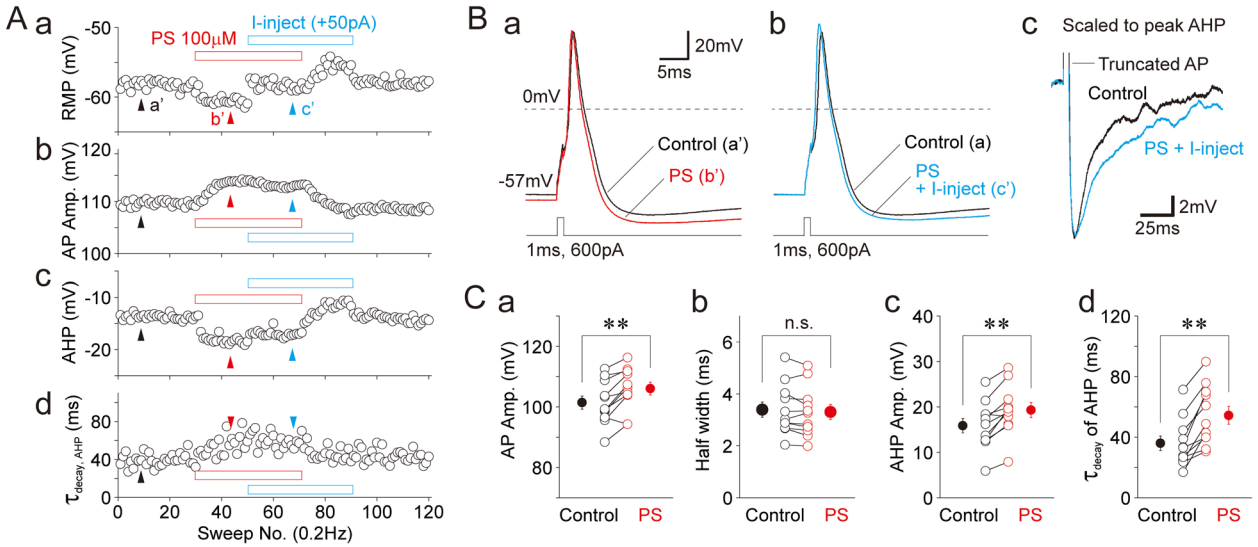

Fig. 9 Effect of PS on the shape of single action potentials. **A**, Typical time courses showing the resting membrane potential (RMP; **a**), action potential (AP) amplitude (**b**), amplitude of afterhyperpolarization (AHP; **c**), and decay time constant (τ_{decay}) of afterhyperpolarization (**d**) before, during, and after the application of 100 μM PS. The PS-induced membrane hyperpolarization was reversed by applying depolarizing direct current (+ 50 pA, cyan trace). Action potentials were elicited by strong and brief depolarizing current stimuli (600 pA, 1 ms duration). **B**, **a**, Typical raw traces of single action potentials elicited by brief depolarizing current stimuli in the absence (**a'**) and presence (**b'**) of 100 μM PS, and in the presence of 100 μM PS plus depolarizing DC current (**c'**), as indicated by arrowheads in **A**. **b**, Typical raw traces of afterhyperpolarization elicited by brief depolarizing current stimuli in the absence (black trace) and in the presence of 100 μM PS plus depolarizing DC current (cyan trace). **C**, Changes induced by 100 μM PS in the amplitude (**a**) and half-width (**b**) of action potentials, the amplitude of afterhyperpolarization (**c**), and the decay time constant of afterhyperpolarization (**d**). Open circles represent individual results ($n = 11$); bars indicate the mean and standard error of the mean. $^{**}p < 0.01$; n.s., not significant (paired t-test)

membrane potential (Fig. 9Aa), it slightly but significantly increased the amplitude of action potentials to 104.6% ± 1.1% of the control ($n = 11$, $p < 0.01$; Fig. 9Ab, Ca). Adjusting membrane potentials by adding depolarizing DC current did not affect the PS-induced increase in action potential amplitude (Fig. 8Ab, Bb), suggesting that the direct potentiation of TTX-R Na + channels by PS may underlie this effect. However, PS (100 μM) had no notable effect on the half-width of action potentials (Fig. 9Cb). PS (100 μM) also increased the amplitude of afterhyperpolarization to 124.3% ± 4.7% of the control ($n = 11$, $p < 0.01$; Fig. 9Ac, Cc). Adjusting membrane potentials by adding depolarizing DC current did not affect the PS-induced increase in the amplitude of afterhyperpolarization (Fig. 9Ac, Bb). Voltage-gated K^+ channels might be involved in the PS-induced increase in the amplitude of afterhyperpolarization because PS (100 μM) slightly but significantly increased voltage-gated I_K, such as the rapidly inactivating A-type and the slowly inactivating delayed rectifier I_K (Fig. S12A–D). PS (100 μM) also increased the decay time constant (τ_{decay}) of afterhyperpolarization to 158.9% ± 13.3% of the control ($n = 11$, $p < 0.01$; Fig. 9Ad, Cd). Adjusting membrane potentials by depolarizing DC current did not affect the τ_{decay} of afterhyperpolarization (Fig. 9Ad, Bc). Several ion channels, such as hyperpolarization-activated and cyclic nucleotide–gated cation (HCN) channels and small-conductance Ca^{2+}-activated K^+ (SK) channels, can be involved in the depolarizing phase following hyperpolarization [47, 48]. However, we found that PS had no effect on the sag potential—which is mediated by activation of HCN channels—or on the time constant of the depolarizing phase following hyperpolarization (Fig. S13A, B). Additionally, PS still increased the τ_{decay} of afterhyperpolarization even in the presence of 100 nM apamin, a selective SK channel blocker [49] (Fig. S13C, D), suggesting that the involvement of HCN and SK channels in the PS-induced change in the shape of afterhyperpolarization is negligible. On the other hand, DHEA (100 μM) had no effect on the shape of action potentials (Fig. S11F) and several types of voltage-gated I_K (Fig. S12E, F).

Discussion

PS modulation of TTX-R Na^+ channels in dural afferent neurons

In the present study, we found that PS slightly but significantly increased the amplitude of TTX-R I_{NaT} in a

concentration-dependent manner. To the best of our knowledge, this is the first evidence demonstrating the positive modulation of TTX-R I_{NaT} by the excitatory neurosteroid PS, as a previous study showed that PS inhibits the I_{Na} mediated by recombinant $Na_V1.2$ expressed in *Xenopus* oocytes [50]. Since pregnanolone sulfate, which is structurally similar to PS, is reported to increase the I_{Na} mediated by recombinant $Na_V1.8$ but decrease currents through $Na_V1.2$, $Na_V1.6$, and $Na_V1.7$ [51], the modulation of voltage-gated Na^+ channels by PS appears to depend on the Na^+ channel subtype.

In addition to its effect on TTX-R I_{NaT}, PS further potentiated TTX-R I_{NaP} and I_{Ramp} in a concentration-dependent manner. The potentiation of TTX-R I_{NaP} by PS may be due to impaired channel inactivation, as PS increased τ_{slow} and decreased A_{slow} of TTX-R I_{NaT}, respectively. In central neurons, I_{NaP} is implicated in the subthreshold generation of action potentials as well as in their regular and repetitive firing [43–45]. Our recent study has also demonstrated that TTX-R I_{NaP} contributes to the repetitive generation of action potentials in dural afferent neurons [23]. Pathologically, I_{NaP} is closely associated with several neurological disorders involving excessive neuronal excitability, such as epilepsy and pain [52, 53]. I_{NaP} is likely involved in migraine headaches, as suggested by a recent study showing that GS-967, a specific late I_{Na} inhibitor, reduced spreading depression–evoked allodynia in a mouse model of migraine with aura [24]. Moreover, GS-967 has been shown to inhibit the elevated I_{NaP} found in type 3 familial hemiplegic migraine with $Na_V1.1$ mutations [54]. In this context, we have previously shown that propranolol (a β-blocker) and amitriptyline (a tricyclic antidepressant) preferentially inhibit TTX-R I_{NaP}, thereby decreasing the excitability of dural afferent neurons [21, 22], indicating that TTX-R I_{NaP} may be a potential pharmacological target for migraine treatment. Considering that the density of TTX-R I_{NaP} is increased by inflammatory mediators [23] and that PS potentiated TTX-R I_{NaP} in dural afferent neurons, PS may exert a pronociceptive effect in migraine headaches by enhancing TTX-R I_{NaP}.

The PS-induced increase in TTX-R I_{NaP} may result in changes in channel properties and thus neuronal excitability, as the density of TTX-R I_{NaP} is correlated with various properties of TTX-R Na^+ channels, such as voltage-inactivation relationships, use-dependent inhibition, and inactivation and recovery kinetics [23]. Indeed, we found that PS shifted the voltage-activation and voltage-inactivation relationships to hyperpolarized and depolarized ranges, respectively, indicating that TTX-R Na^+ channels are activated by lower voltage stimulation and are less inactivated even at more depolarized membrane potentials. We also found that PS increased the τfast value for inactivation kinetics and decreased it for recovery kinetics. These results indicate that PS retarded the onset of inactivation during sustained membrane depolarization and accelerated recovery after channel inactivation. All of these findings may support the PS-induced decrease in the extent of use-dependent inhibition of TTX-R Na^+ channels. Taken together, our results suggest that PS acts as an excitatory neuromodulator of TTX-R Na^+ channels and increases the excitability of dural afferent neurons.

On the other hand, we found that PS potentiated the current mediated by $Na_V1.9$, another TTX-R Na^+ channel subtype expressed in nociceptive sensory neurons [17]. $Na_V1.9$ has also been implicated in inflammatory hyperalgesia, as inflammatory mediators, including prostaglandin E_2, potentiate the $Na_V1.9$-mediated current [55, 56]. Given that a recent study has shown the possible involvement of $Na_V1.9$ in triptan-overuse headache [57], it would be of great interest to investigate whether the PS potentiation of $Na_V1.9$ is involved, at least in part, in the pronociceptive effect on migraine headaches.

It should also be noted that DHEA, in contrast to PS, decreased TTX-R I_{Na} in a concentration-dependent manner. As shown in Fig. 1A, PS and DHEA differ from pregnenolone at positions 3 and 17, respectively, and thus changes at position 3 (sulfation by sulfotransferase) lead to an increase in TTX-R I_{Na}, whereas changes at position 17 (oxidation by P450c17) lead to a decrease in TTX-R I_{Na}. This speculation may be further supported by our finding that DHEAS, which differ from pregnenolone at positions both 3 and 17, had little effect on TTX-R I_{Na}, suggesting that DHEAS may have both positive and negative effects on TTX-R Na^+ channels.

PS-induced changes in the excitability of dural afferent neurons

It is well known that PS acts as an excitatory neuromodulator in the central nervous system [4]. These effects are mainly attributed to the potentiation of excitatory NMDA receptors or inhibition of inhibitory $GABA_A$ receptors [5, 7]. However, little is known about the roles of PS in the excitability of nociceptive sensory neurons. Our present results suggest that PS has a complex effect on the excitability of small-sized nociceptive neurons. First, PS directly hyperpolarized small-sized dural afferent neurons in a concentration-dependent manner. The PS-induced membrane hyperpolarization was accompanied by a decrease in input resistance, consistent with the existence of a PS-induced membrane conductance. Voltage-clamp experiments revealed that the equilibrium potential of the PS-induced current was very close to the theoretical K^+ equilibrium potential, indicating that PS hyperpolarized dural afferent neurons by increasing leak

K^+ conductance, which may be mediated by acid-sensitive K2P channel subtypes, such as TASK-1 and TASK-3. Since multiple types of K2P channels are functionally expressed in nociceptive sensory neurons [58], it would be of great interest to investigate whether PS modulates other K2P channel subtypes involved in determining resting membrane potentials.

Second, PS significantly decreased the amplitude of rheobase current, consistent with a decrease in the threshold for action potential generation. Since PS-induced membrane hyperpolarization and decreased input resistance are generally expected to increase the threshold for action potential generation, other counteracting effects must be responsible for the PS-induced decrease in rheobase current amplitude. The potentiation of TTX-R Na^+ channels could explain the PS-induced decrease in rheobase current amplitude, as PS increased the amplitude of single action potentials. Although the mechanisms are not fully elucidated, the PS-induced decrease in the threshold for action potential generation could contribute to the generation of pain signals in response to sub-nociceptive stimuli, a hallmark of allodynia [59].

Third, PS increased the number of action potentials elicited by depolarizing current stimuli above threshold. Our present results suggest that TTX-R I_{NaP} was critically responsible for the PS-induced increase in the number of action potentials. Similarly, I_{NaP} is involved in repetitive and regular firing of action potentials in a number of central neurons [44, 60, 61]. Given that PS greatly potentiated I_{NaP} and affected the kinetics of inactivation and recovery of TTX-R Na^+ channels, it is highly plausible that the PS-mediated potentiation of TTX-R I_{NaP} is responsible for the increased excitability of dural afferent neurons. Therefore, the PS-induced increase in the number of action potentials suggests that PS might contribute to hyperalgesia in response to suprathreshold nociceptive stimuli [59]. Other ion channels, such as voltage-gated K^+ channels and HCN channels, may be involved in the PS-induced increase in the number of action potentials, as these channels contribute to the frequency of action potentials in nociceptive neurons [62, 63]. However, we found that PS had a minor effect on the fast-inactivating A-type I_K and non-inactivating delayed rectifier I_K mediated by several voltage-gated K^+ channel subtypes, and it had no effect on sag potential mediated by HCN channels. Taken together, these results show that PS exerts complex effects on the excitability of dural afferent neurons by acting on a range of ion channels, involving both inhibitory and excitatory mechanisms.

Possible association of neurosteroids with migraine pathology

PS may be involved in migraine pathology because it activates TRPM3 to release calcitonin gene-related peptide [16], which is a key molecule known to induce neurogenic inflammation in migraine pathology [64]. Furthermore, a recent study has shown that PS acts on mechanosensitive TRPM3 to increase the activity of TG nerves innervating the meninges [65]. Our present results provide additional evidence that PS has a pronociceptive effect on migraine headaches by increasing the excitability of dural afferent neurons through the potentiation of TTX-R Na^+ channels. In this regard, it should be noted that plasma levels of PS range from submicromolar to low micromolar concentrations in humans [66], indicating that plasma concentrations of PS may not be sufficient to modulate TTX-R Na^+ channels. Additionally, a recent study has shown that serum levels of PS were significantly lower in the menstruation-related migraine group than in controls [67]. Nevertheless, the actual concentration of local PS around the trigeminovascular system involved in the nociceptive pathway of migraine headaches remains unknown. In fact, the concentration of endogenous PS-like neurosteroid released from depolarized rat hippocampal CA1 neurons has been reported to be equivalent to 17 μM of exogenously applied PS [32]. At equivalent concentrations (10–30 μM), PS could modulate TTX-R Na^+ channels and neuronal excitability, as shown in the present study. Further studies are needed to determine the local concentration of PS within the trigeminovascular system, including the dura mater and dural afferent neurons.

In the present study, we found that transcripts for all enzymes involved in the synthesis and transport of neurosteroids acting on TTX-R Na^+ channels were detected in the ophthalmic branch of the TG, suggesting that both PS and DHEA can be locally synthesized within this region. In this context, it is noteworthy that DHEA, but not pregnenolone, significantly decreased both TTX-R I_{NaT} and I_{NaP} mediated by $Na_V1.8$. DHEA also potently inhibited the $Na_V1.9$-mediated current. These results suggest that locally generated PS and DHEA, if present, could regulate the excitability of dural afferent neurons via the opposite modulation of TTX-R Na^+ channels. As a previous study has shown that DHEA levels are reduced in patients with chronic migraine [68], it would also be of great interest to investigate whether the functional expression of SULT2B1, P450c17, and STS—involved in the biosynthesis and hydrolysis of PS and DHEA—is associated with migraine pathology.

Limitation of the present study

Although the present study has demonstrated the effects of neurosteroids on the excitability of dural afferent neurons, there are several limitations to the translation of our findings to clinical aspects. First, although we have demonstrated the expression of several enzymes involved in neurosteroidogenesis in the ophthalmic branch of the trigeminal ganglia, the actual neurosteroid concentrations in the dural mater and trigeminal ganglia are still unknown. In this context, further studies are needed to determine the levels of neurosteroids, particularly PS and DHEA, in human tissues involved in migraine pathology. It would also be interesting to examine whether PS and DHEA levels change with migraine attack and severity. This information may help to develop new biomarkers or therapeutic targets for migraine treatment. Second, although our study showed that endogenous PS did not modulate TTX-R Na^+ channels, this may be due to our experimental conditions, such as in isolated single neurons. It would be interesting to determine whether endogenous neurosteroids can modulate TTX-R Na^+ channels under more intact conditions, such as in tissue slice preparations or in vivo conditions. Finally, we have demonstrated the effects of PS and DHEA on TTX-R Na^+ channels, but the role of other ion channels modulated by neurosteroids in dural afferent neurons should be further investigated. For example, $Na_V1.7$, which is specifically expressed in nociceptive neurons [17], and other TTX-sensitive Na^+ channel subtypes may be potential targets for the neurosteroid modulation. Additionally, since $GABA_A$, NMDA, σ1 receptors, and TRPM3 are also expressed in nociceptive sensory neurons [17, 69–71], the neurosteroid modulation of these receptors and ion channels may affect the excitability of dural afferent neurons. These findings highlight the need for further research to fully understand the role of neurosteroids in migraine pathophysiology and to explore their potential as therapeutic targets.

Conclusion

In the present study, we have demonstrated that the excitatory neurosteroid PS preferentially potentiated TTX-R I_{NaP} and modulated TTX-R Na^+ channels to reduce their inactivation, resulting in increased excitability of dural afferent neurons. The inhibitory neurosteroid DHEA had opposite effects on TTX-R Na^+ channels and neuronal excitability in these neurons. Since all transcripts for enzymes and transporters involved in the biosynthesis and membrane transport of PS and DHEA were detected in the ophthalmic branch of the TG, these findings suggest that neurosteroids, particularly PS and DHEA, play crucial roles in regulating the excitability of dural afferent neurons and may be involved in migraine pathophysiology.

Abbreviations

3β-HSD	3β-hydroxysteroid dehydrogenase
DHEA	Dehydroepiandrosterone
DHEAS	Dehydroepiandrosterone sulfate
I_A	A-type K^+ current
I_{DR}	delayed rectifier K^+ current
I_K	K^+ current
I_{Na}	Na^+ current
I_{NaP}	Persistent Na^+ current
I_{NaT}	Transient Na^+ current
I_{Ramp}	Slow voltage ramp-induced Na^+ current
K2P channel	Two-pore domain K^+ channel
OST-α	Organic solute transporter-α
P450c17	Steroid 17α-hydroxylase
P450scc	Cytochrome P450 side-chain cleavage
PGE_2	Prostaglandin E_2
PS	Pregnenolone sulfate
STS	Steroid sulfatase
SULT	Sulfotransferase
TRPM3	Transient receptor potential melastatin 3
TRPV1	Transient receptor potential vanilloid 1
τ_{decay}	Decay time constant
τ_{fast}	Fast time constant
$\tau_{intermediate}$	Intermediate time constant
τ_{slow}	Slow time constant
$\tau_{weighted}$	Weighted time constant
TG	Trigeminal ganglia
TSPO	Translocator protein
TTX-R	Tetrodotoxin-resistant
TTX-S	Tetrodotoxin-sensitive
$V_{50,\ activation}$	Midpoint voltage for activation
$V_{50,\ inactivation}$	Midpoint voltage for inactivation

Supplementary Information

The online version contains supplementary material available at https://doi.org/10.1186/s10194-025-01968-7.

Supplementary Material 1: Figure S1. Expression of 3β-HSD and SULT2A1 in the liver, testis, and adrenal gland. Total RNA was extracted from each tissue. 3β-HSD and SULT2A1 were clearly detected in the adrenal gland and liver, respectively, confirming the effectiveness of the primers used to detect these enzymes. Figure S2. Property of small-sized DiI-positive neurons. A, Typical phase contrast (Ph) and fluorescence (DiI) images of small-sized DiI-positive neurons. B, Typical raw traces of voltage-gated Na^+ currents observed from small-sized DiI-positive neurons in the absence and presence of 300 nM TTX. Voltage-gated Na^+ currents were elicited by brief voltage step pulses (100 ms duration, −80 mV to −10 mV) in the presence of 100 μM Cd^{2+}. C, a, A typical raw trace observed from small-sized DiI-positive neurons before, during, and after the application of 500 nM capsaicin at a holding potential of −80 mV. b, The proportion of capsaicin-positive small-sized DiI-positive neurons. DiI-positive neurons eliciting a capsaicin-induced membrane current of ≥100 pA were considered capsaicin-positive neurons. The brackets represent the number of capsaicin-positive neurons and all neurons tested. Figure S3. Effects of PS and DHEA on the decay phase of TTX-R I_{NaT}. A, a, Typical raw traces of TTX-R I_{Na} recorded in the absence (black trace) and presence (red trace) of 100 μM PS. TTX-R I_{Na} was elicited by brief voltage step pulses (100 ms duration, −80 mV to −10 mV). Insets show I_{Na} with expanded time (i) and amplitude (ii) scales. b, PS-induced changes in the weighted decay time constant ($\tau_{weighted}$). Open circles represent individual results ($n = 10$); closed circles and error bars indicate the mean and standard error of the mean (SEM). $^{**}p < 0.01$ (paired t-test). B, PS-induced changes in τ_{fast} (a), $\tau_{intermediate}$ (b), τ_{slow} (c), A_{fast} (d), $A_{intermediate}$ (e), and A_{slow} (f). Open circles represent individual results ($n = 10$); closed circles and error bars indicate the mean and SEM. $^{*}p < 0.05$; $^{**}p < 0.01$; n.s., not significant (paired t-test). C, a, Typical raw traces of TTX-R I_{Na} recorded in the absence (black trace) and presence (cyan trace) of 100 μM DHEA. TTX-R I_{Na} was elicited by brief voltage step pulses (100 ms duration, −80 mV to −10 mV). Insets show I_{Na} with expanded time (i) and amplitude (ii) scales. b, DHEA-induced

changes in the weighted decay time constant ($\tau_{weighted}$). Open circles represent individual results ($n = 10$); closed circles and error bars indicate the mean and SEM. n.s., not significant (paired t-test). D, DHEA-induced changes in τ_{fast} (a), $\tau_{intermediate}$ (b), τ_{slow} (c), A_{fast} (d), $A_{intermediate}$ (e), and A_{slow} (f). Open circles represent individual results ($n = 10$); closed circles and error bars indicate the mean and SEM. n.s., not significant (paired t-test). Figure S4. Effects of BD-1047 and ononetin on DHEA-induced changes in the amplitude of TTX-R I_{NaT}, I_{NaP}, and I_{Ramp}. A, Representative traces of TTX-R I_{NaT} and I_{NaP} obtained before and after the application of 100 μM DHEA in the presence of 100 nM BD-1047, a selective σ1 receptor antagonist. TTX-R I_{Na} was elicited by brief voltage step pulses (100 ms duration, −80 mV to −10 mV). B, DHEA (100 μM)–induced changes in the amplitude of TTX-R I_{NaT} (left) and I_{NaP} (right) in the absence and presence of 100 nM BD-1047 (a) or 10 μM ononetin, a TRPM3 antagonist (b). Open circles represent individual results ($n = 8$); closed circles and error bars indicate the mean and SEM. n.s., not significant (paired t-test). C, a, Representative traces of TTX-R I_{Ramp} obtained before and after the application of 100 μM DHEA in the presence of 10 μM ononetin. TTX-R I_{Ramp} was elicited by slow voltage-ramp stimulation (−80 mV to +10 mV at 15 mV/s, every 20 s). b, DHEA (100 μM)–induced changes in the amplitude of TTX-R I_{Ramp} in the absence and presence of 100 nM BD-1047 (left) or 10 μM ononetin (right). Open circles represent individual results ($n = 8$); closed circles and error bars indicate the mean and standard error of the mean. n.s., not significant (paired t-test). Figure S5. Effects of intracellular PS or γ-cyclodextrin on PS-induced changes in the amplitude of TTX-R I_{NaT}, I_{NaP}, and I_{Ramp}. A, a, Schematic illustration for testing the effect of intracellular application of PS. In this experiment, PS (100 μM) was added into the pipette solution. b, Representative traces of TTX-R I_{NaT} and I_{NaP} obtained before and after the application of 100 μM PS in the presence of intracellular PS (100 μM). TTX-R I_{Na} was elicited by brief voltage step pulses (100 ms duration, −80 mV to −10 mV). c, Extracellular PS (100 μM)–induced changes in the amplitude of TTX-R I_{NaT} (left) and I_{NaP} (right) in the absence and presence of intracellular PS (100 μM). Open circles represent individual results ($n = 8$); columns and error bars indicate the mean and SEM. n.s., not significant (unpaired t-test). B, a, Representative traces of TTX-R I_{Ramp} obtained before and after the application of 100 μM PS in the presence of intracellular PS (100 μM). TTX-R I_{Ramp} was elicited by slow voltage-ramp stimulation (−80 mV to +10 mV at 15 mV/s, every 20 s). b, Extracellular PS (100 μM)–induced changes in the amplitude of TTX-R I_{Ramp} in the absence and presence of intracellular PS (100 μM). Open circles represent individual results ($n = 8$); columns and error bars indicate the mean and SEM. n.s., not significant (unpaired t-test). C, a, Representative traces of TTX-R I_{NaT} and I_{NaP} obtained before and after the application of 500 μM γ-cyclodextrin (γ-CD), a sequestrator of PS. TTX-R I_{Na} was elicited by brief voltage step pulses (100 ms duration, −80 mV to −10 mV). b, γ-CD (500 μM)–induced changes in the amplitude of TTX-R I_{NaT} (left) and I_{NaP} (right). Open circles represent individual results ($n = 8$); closed circles and error bars indicate the mean and SEM. n.s., not significant (paired t-test). D, a, Representative traces of TTX-R I_{Ramp} obtained before and after the application of 500 μM γ-CD. TTX-R I_{Ramp} was elicited by slow voltage-ramp stimulation (−80 mV to +10 mV at 15 mV/s, every 20 s). b, γ-CD (500 μM)–induced changes in the amplitude of TTX-R I_{Ramp}. Open circles represent individual results ($n = 8$); closed circles and error bars indicate the mean and SEM. n.s., not significant (paired t-test). Figure S6. Effects of PS and DHEA on $Na_V1.9$-mediated current. A, a, Representative traces of TTX- R I_{Na} elicited by depolarizing step pulses (up to −50 mV, 5 mV increments, 100 ms duration) at a holding potential (V_H) of −80 mV (left) or −120 mV (right) in the presence of 300 nM TTX and 100 μM Cd^{2+}. Note that the $Na_V1.9$-mediated current reappeared when V_H was adjusted to −120 mV. b, Voltage-activation relationship of TTX- R I_{Na} at V_H of −80 mV or −120 mV. Each circle and error bar represent the mean and SEM from eight neurons. B, Typical time course of the amplitude of $Na_V1.9$-mediated current recorded before, during, and after the application of PS (100 μM) and DHEA (100 μM). C, a, Representative traces of $Na_V1.9$-mediated current in the absence and presence of 100 μM PS (left) and 100 μM DHEA (right). The $Na_V1.9$-mediated current was elicited by depolarizing step pulses (up to −60 mV, 100 ms duration) at a V_H of −120 mV in the presence of 300 nM TTX and 100 μM Cd^{2+}. b, Changes induced by 100 μM PS (left) or 100 μM DHEA (right) in the amplitude of $Na_V1.9$-mediated current. Open circles represent individual results ($n = 7$ for PS, $n = 7$ for DHEA); closed circles and error bars indicate the mean and SEM. $^{**}p < 0.01$ (paired t-test). D, Concentration–response relationships of PS and DHEA on $Na_V1.9$-mediated current elicited by depolarizing step pulses (−120 mV to −60 mV, 100 ms duration). Each point and error bar represent the mean and SEM from seven neurons for both PS and DHEA. The IC_{50} value of DHEA was 49.2 μM. Figure S7. Effect of DHEA on the voltage dependence of TTX-R Na^+ channels. A, Representative traces of TTX-R I_{Na} elicited by voltage step pulses in the absence (left trace) and presence (right trace) of 100 μM DHEA. TTX-R I_{Na} was induced by 100 ms depolarizing pulses in 10 mV increments from a holding potential of −80 mV. B, a, Voltage-activation relationship of TTX-R Na^+ channels in the absence (black circles) and presence (red circles) of 100 μM DHEA. Continuous lines represent the best fit to the Boltzmann function. Each point and error bar represent the mean and standard error of the mean (SEM) from 10 neurons. b, Changes induced by 100 μM DHEA in the midpoint voltage for activation ($V_{50,activation}$) of TTX-R Na^+ channels. Open circles connected by lines represent individual results ($n = 10$), whereas closed circles and error bars indicate the mean and SEM. $^{**}p < 0.01$ (paired t-test). c, Concentration–response relationship of DHEA on $V_{50,activation}$. Open circles represent individual results ($n = 10$ for each concentration); columns and error bars indicate the mean and SEM. $^{**}p < 0.01$; n.s., not significant (paired t-test). C, Representative raw traces of TTX-R I_{Na} elicited by voltage step pulses in the absence (left trace) and presence (right trace) of 100 μM DHEA. TTX-R I_{Na} was induced by 50 ms depolarizing pulses from −120 mV to−10 mV in 10 mV increments from a holding potential of −80 mV. D, a, Steady-state fast inactivation relationship of TTX-R Na^+ channels in the absence (black circles) and presence (red circles) of 100 μM DHEA. Continuous lines represent the best fit to the Boltzmann function. Each point and error bar represent the mean and SEM from 10 neurons. b, Changes induced by 100 μM DHEA in the midpoint voltage for inactivation ($V_{50,inactivation}$) of TTX-R Na^+ channels. Open circles connected by lines represent individual results ($n = 10$), whereas closed circles and error bars indicate the mean and SEM. $^{**}p < 0.01$ (paired t-test). c, Concentration–response relationship of DHEA on $V_{50,inactivation}$. Open circles represent individual results ($n = 10$ for each concentration); columns and error bars indicate the mean and SEM. $^{**}p < 0.01$; n.s., not significant (paired t-test). E, Representative raw traces of TTX-R I_{Na} elicited by voltage step pulses for slow inactivation of TTX-R Na^+ channels in the absence (left trace) and presence (right trace) of 100 μM DHEA. TTX-R I_{Na} was induced by conditioning prepulses (5 s duration, −100 mV to −10 mV, 10 mV increments) followed by 50 ms test pulses (−80 mV to −10 mV) with an interval of 20 ms. F, a, Slow inactivation relationship of TTX-R Na^+ channels in the absence (black circles) and presence (red circles) of 100 μM DHEA. Continuous lines represent the best fit to the Boltzmann function. Each point and error bar represent the mean and SEM from 10 neurons. b, Changes induced by 100 μM DHEA in the midpoint voltage for slow inactivation ($V_{50,inactivation}$) of TTX-R Na^+ channels. Open circles connected by lines represent individual results ($n = 10$), whereas closed circles and error bars indicate the mean and SEM. $^{**}p < 0.01$ (paired t-test). c, Concentration–response relationship of DHEA on $V_{50,inactivation}$. Open circles represent individual results ($n = 10$ for each concentration); columns and error bars indicate the mean and SEM. n.s., not significant (paired t-test). Figure S8. Effect of DHEA on the use-dependent inhibition of TTX-R Na^+ channels. A, Representative raw traces of TTX-R I_{Na} elicited by voltage step pulses at 10 Hz in the absence (left trace) and presence (right trace) of 100 μM DHEA. Each pulse sequence consisted of depolarizing steps from −80 mV to −10 mV with a 10 ms duration, applied continuously for 20 s. B, Time courses of the TTX-R I_{Na} peak amplitude during a train of 40 pulses at 2 Hz (a), 100 pulses at 5 Hz (b), and 200 pulses at 10 Hz (c), in the absence and presence of 100 μM DHEA. The peak amplitudes of all TTX-R I_{Na} pulses (P_n) were normalized to that of the first pulse (P_1). Each point and error bar represent the mean and standard error of the mean (SEM) from eight neurons (2 Hz), nine neurons (5 Hz), and 10 neurons (10 Hz). C, DHEA (100 μM)–induced changes in the P_{40}/P_1 (2 Hz, a), P_{100}/P_1 (5 Hz, b), and P_{200}/P_1 (10 Hz, c) ratios of TTX-R Na^+ channels. Open circles connected by lines represent the individual results ($n = 8$ for 2 Hz, n = 9 for 5 Hz, $n = 10$ for 10 Hz), whereas closed circles and error bars indicate the mean and SEM. n.s, not significant (paired t-test). D, DHEA (100 μM)–induced changes in the P_{last}/P_1 ratios. Open circles represent individual results ($n = 8$ for 2 Hz, $n = 9$ for 5 Hz, $n = 10$ for 10 Hz), whereas columns and error bars indicate the mean

and SEM. n.s., not significant (paired t-test). b, Concentration-response relationships of DHEA against the use-dependent inhibition of TTX-R Na^+ channels (10 Hz). Open circles represent individual results ($n = 7$ for 10 μM, $n = 7$ for 30 μM, and $n = 10$ for 100 μM), with columns and error bars indicating the mean and SEM. n.s., not significant (paired t-test). Figure S9. Effect of PS on parameters for inactivation and recovery kinetics of TTX-R Na^+ channels. A, PS (100 μM)–induced changes in the kinetic parameters for the development of inactivation of TTX-R Na^+ channels: a; τ_{fast}, b; τ_{slow}, c; A_{fast}, d; A_{slow}. Open circles represent the individual results ($n = 11$); closed circles and error bars indicate the mean and SEM. $^{**}p < 0.01$ (paired t-test). B, PS (100 μM)–induced changes in the kinetic parameters for the recovery from inactivation of TTX-R Na^+ channels: a; τ_{fast}, b; $\tau_{intermediate}$, c; τ_{slow}, d; A_{fast}, e; $A_{intermediate}$, f; A_{slow}. Open circles represent the individual results ($n = 10$); closed circles and error bars indicate the mean and SEM. $^{**}p < 0.01$ (paired t-test); n.s., not significant (paired t-test). Figure S10. Effect of DHEA on the inactivation and recovery kinetics of TTX-R Na^+ channels. A, a, Schematic illustration of voltage step pulses used to study the development of inactivation of TTX-R Na^+ channels. b, Representative raw traces of the second TTX-R I_{Na} (P_2) elicited by voltage step pulses in the absence (left trace) and presence (right trace) of 100 μM DHEA. Dotted lines represent the first TTX-R I_{Na} (P_1). B, Kinetics of the development of TTX-R Na^+ channel inactivation in the absence (black circles) and presence (red circles) of 100 μM DHEA. The P_2/P_1 ratio was plotted against prepulse duration. Continuous lines represent the best fit to a double exponential function. Each point and error bar represent the mean and SEM from nine neurons. C, Concentration-response relationship of DHEA against the τ_{fast} of inactivation kinetics. Open circles represent the individual results ($n = 9$ for each concentration), whereas columns and error bars indicate the mean and SEM. $^{*}p < 0.05$; n.s, not significant (paired t-test). D, Concentration–response relationship of DHEA on the fast time constant (τ_{fast}) of inactivation kinetics. Open circles represent individual results ($n = 9$ for each concentration); columns and error bars indicate the mean and SEM. $^{*}p < 0.05$; n.s., not significant (paired t-test). E, a, Schematic illustration of voltage step pulses used to study recovery from TTX-R Na^+ channel inactivation. b, Representative raw traces of the second TTX-R I_{Na} (P_2) elicited by voltage step pulses in the absence (left trace) and presence (right trace) of 100 μM DHEA. Dotted lines represent the first TTX-R I_{Na} (P_1). F, Kinetics of recovery from TTX-R Na^+ channel inactivation in the absence (black circles) and presence (red circles) of 100 μM DHEA. The P_2/P_1 ratio was plotted against the duration of the recovery interval. Continuous lines represent the best fit to a triple exponential function. Each point and error bar represent the mean and SEM from nine neurons. G, Concentration–response relationship of DHEA on the fast time constant (τ_{fast}) of recovery kinetics. Open circles represent individual results ($n = 9$ for each concentration); columns and error bars indicate the mean and SEM. $^{**}p < 0.01$ (paired t-test); n.s., not significant (paired t-test). H, DHEA (100 μM)–induced changes in the kinetic parameters for the recovery from inactivation of TTX-R Na^+ channels: a; τ_{fast}, b; $\tau_{intermediate}$, c; τ_{slow}, d; A_{fast}, e; $A_{intermediate}$, f; A_{slow}. Open circles represent individual results ($n = 9$); closed circles and error bars indicate the mean and SEM. $^{**}p < 0.01$; n.s., not significant (paired t-test). Figure S11. Effect of PS on the membrane current of small-sized DiI-positive neurons. A, a, Typical current traces recorded before, during, and after the application of 100 μM PS at various holding potentials (V_H; −120 mV to +40 mV). The intracellular and extracellular K^+ concentrations ($[K^+]_i$ and $[K^+]_o$) were 150 mM and 153 mM, respectively. b, Current–voltage relationships of the PS-induced current. The K^+ equilibrium potential (E_K; indicated by arrows) was −85.7 mV for $[K^+]_o = 5$ mM (vermilion) and +0.5 mV for $[K^+]_o = 153$ mM (cyan), as calculated using the Nernst equation. Points and error bars represent the mean and standard error of the mean (SEM) from six neurons for each $[K^+]_o$ condition. B, a, A typical current trace recorded before, during, and after the application of 100 μM PS in the absence (black trace) and presence (red trace) of 100 nM BD-1047, a selective σ1 receptor antagonist. b, BD-1047–induced changes in the PS-induced current (I_{PS}). Open circles connected by lines represent individual results ($n = 7$); closed circles and error bars indicate the mean and SEM. n.s., not significant (paired t-test). C, a, A typical current trace recorded before, during, and after the application of 100 μM PS in the absence and presence of an acidic extracellular solution (pH 6.0; indicated by a horizontal bar). b, Acidic pH (pH 6.0)–induced changes in the I_{PS}. Open circles connected by lines represent individual results ($n = 7$); closed circles and error bars indicate the mean and SEM. $^{**}p < 0.01$ (paired t-test). D, a, A typical current trace recorded before, during, and after the application of 100 μM PS in the absence and presence of 1 μM A-1899, a TASK-1/TASK-3 inhibitor. b, A-1899 (1 μM)–induced changes in the I_{PS}. Open circles connected by lines represent individual results ($n = 7$); closed circles and error bars indicate the mean and SEM. $^{**}p < 0.01$ (paired t-test). Figure S12. Effect of DHEA on the excitability of small-sized DiI-positive neurons. A, a, A typical raw trace exhibiting spontaneous action potentials recorded before, during, and after the application of 100 μM DHEA under current-clamp conditions. b, Changes induced by 100 μM DHEA in action potential (AP) frequency. Open circles represent individual results ($n = 8$); closed circles and error bars indicate the mean and standard error of the mean (SEM). n.s., not significant (paired t-test). c, Concentration–response relationship of DHEA on AP frequency. Open circles represent individual results ($n = 8$ for each concentration); columns and error bars indicate the mean and SEM. n.s., not significant (paired t-test). B, Representative raw traces recorded in response to four successive depolarizing current stimuli (40 pA increments, 500 ms duration) in the absence (left trace) and presence (right trace) of 100 μM DHEA. C, a, Changes induced by 100 μM DHEA in rheobase current. Open circles represent individual results ($n = 10$); closed circles and error bars indicate the mean and SEM. n.s., not significant (paired t-test). b, Concentration–response relationship of DHEA on rheobase current. Open circles represent individual results ($n = 10$ for each concentration); columns and error bars indicate the mean and SEM. n.s., not significant (paired t-test). c, Concentration–response relationship of DHEA on the membrane potentials of small-sized DiI-positive neurons. Open circles represent individual results ($n = 10$ for each concentration); columns and error bars indicate the mean and SEM. n.s., not significant (paired t-test). D, Representative raw traces recorded in response to four successive depolarizing current stimuli (1T–4T; 1T = 110 pA, 1 s duration) in the absence (left trace) and presence (right trace) of 100 μM DHEA. E, a, Changes induced by 100 μM DHEA in the number of action potentials elicited by depolarizing current stimuli. Open circles represent individual results ($n = 10$); closed circles and error bars indicate the mean and SEM. $^{*}p < 0.05$ (paired t-test). b, Concentration–response relationship of DHEA on the number of action potentials elicited by depolarizing current stimuli (4T). Open circles represent individual results ($n = 10$ for each concentration); columns and error bars indicate the mean and SEM. $^{*}p < 0.05$; n.s., not significant (paired t-test). F, Representative raw traces of single action potentials elicited by brief depolarizing current stimuli in the absence (black trace) and presence (cyan trace) of 100 μM DHEA. Action potentials were elicited by strong and brief depolarizing current stimuli (600 pA, 1 ms duration). Figure S13. Effects of PS and DHEA on voltage-gated I_K. A, a, Typical current traces recorded in response to depolarizing voltage steps (−120 mV to +60 mV, 1 s duration) in the absence (left trace) and presence (right trace) of 100 μM PS. b, Superimposed current traces scaled to the peak amplitude. B, a, PS (100 μM)–induced changes in voltage-gated I_K. Open circles represent individual results ($n = 8$), whereas closed circles and error bars indicate the mean and SEM. $^{**}p < 0.01$ (paired t-test). b, PS (100 μM)–induced changes in the weighted decay time constant ($\tau_{weighted}$) of the voltage-gated K^+ current. Open circles represent individual results ($n = 8$); closed circles and error bars indicate the mean and SEM. $^{**}p < 0.01$; n.s., not significant (paired t-test). C, a, Separation of fast-inactivating A-type (I_A) and non-inactivating delayed rectifier (I_{DR}) I_K using two voltage step pulses (lower panel). Depolarizing voltage step pulses (−120 mV to+60 mV, 1 s duration) were applied to patched neurons with (b′) or without (a′) a prepulse (−20 mV, 1 s duration) at an interval of 20 s. Subtraction of the two current traces (middle panel; a′–b′) yielded the I_A component (red trace). b, Typical current traces of I_{DR} (left) and I_A (right) in the absence and presence of 100 μM PS. D, PS (100 μM)–induced changes in the amplitude of I_{DR} (a) and I_A (b). Each point reflects the mean and SEM from seven neurons. Open circles represent individual results ($n = 8$), whereas closed circles and error bars indicate the mean and SEM. $^{*}p < 0.05$; $^{**}p < 0.01$ (paired t-test). E, Typical traces of I_K (a), I_{DR} (b), and I_A (c) in the absence and presence of 100 μM DHEA. F, DHEA (100 μM)–induced changes in the amplitude of I_K (a), I_{DR} (b), and I_A (c). Open circles represent individual

results (n= 8), whereas closed circles and error bars indicate the mean and SEM. n.s., not significant (paired t-test). Figure S14. Effects of PS on sag potential or afterhyperpolarization of single action potentials. A, a, Schematic depiction of five sequential hyperpolarizing current stimuli (−20 pA increments, 1 s duration) used to elicit sag potentials. b, Representative traces of sag potentials in response to hyperpolarizing current stimuli (up to −100 pA, −20 pA increments, 1 s duration), with the sag potential indicated by an arrow. c, A typical trace elicited by a hyperpolarizing current stimulus (−100 pA, 1 s duration), showing the sag potential's amplitude (arrow) and decay phase (highlighted in cyan). The decay phase of the sag potential was fitted to a single-exponential function. B, a, Representative traces elicited by hyperpolarizing current stimuli (−100 pA, 1 s duration) in the absence and presence of 100 μM PS. b, PS (100 μM)–induced changes in the amplitude of the sag potential. Open circles represent individual data points (n = 8), with closed circles and error bars indicating the mean and SEM. n.s., not significant (paired t-test). c, PS (100 μM)–induced changes in the decay time constant (τ_{decay}) of the sag potential. Open circles indicate individual results (n = 8), with closed circles and error bars representing the mean and SEM. n.s., not significant (paired t-test). C, a, Representative traces of afterhyperpolarization (AHP) elicited by brief depolarizing current stimuli (600 pA, 1 ms duration) in the absence and presence of 100 nM apamin, a selective SK channel inhibitor. The depolarizing component of the AP was truncated. The right panel shows two traces scaled to the peak amplitude of the AHP. b, Representative traces of AHPs elicited by brief depolarizing stimuli (600 pA, 1 ms duration) obtained before and after the application of 100 μM PS in the presence of 100 nM apamin. The right panel shows the traces scaled to the peak amplitude of the AHP. D, a, PS (100 μM)–induced changes in AHP amplitude in the presence of 100 nM apamin. Open circles denote individual results (n= 6), with closed circles and error bars indicating the mean and SEM. $^{**}p < 0.01$ (paired t-test). b, PS (100 μM)–induced changes in the decay time constant (τ_{decay}) of AHP in the presence of 100 nM apamin. Open circles represent individual results (n = 6), and closed circles and error bars represent the mean and SEM. $^{**}p<$ 0.01 (paired t-test).

Acknowledgements
Not applicable.

Authors' contributions
ISJ and MN designed the study. ISJ and MN performed the experiments. ISJ and MN wrote the manuscript. ISJ made further critical manuscript revisions. ISJ and MN read and approved the final manuscript.

Funding
This work was supported by the National Research Foundation of Korea (NRF) grant funded by the Korea government (MSIP) (2022R1A2C1091600, RS-2023-00279153, and RS-2024-00405996).

Data availability
No datasets were generated or analysed during the current study.

Declarations

Ethics approval and consent to participate
All experiments were conducted in accordance with approved animal protocols and guidelines established by the Animal Care Committee of Kyungpook National University (Approval No. KNU-2023-0212). Every effort was made to minimize both the number of animals used and their suffering.

Consent for publication
Not applicable.

Competing interests
The authors declare no competing interests.

Received: 14 November 2024 Accepted: 28 January 2025
Published online: 25 February 2025

References

1. Baulieu EE (1998) Neurosteroids: a novel function of the brain. Psychoneuroendocrinology 23:963–987. https://doi.org/10.1016/s0306-4530(98)00071-7
2. Gibbs TT, Russek SJ, Farb DH (2006) Sulfated steroids as endogenous neuromodulators. Pharmacol Biochem Behav 84:555–567. https://doi.org/10.1016/j.pbb.2006.07.031
3. Reddy DS (2010) Neurosteroids: endogenous role in the human brain and therapeutic potentials. Prog Brain Res 186:113–137. https://doi.org/10.1016/B978-0-444-53630-3.00008-7
4. Schumacher M, Liere P, Akwa Y, Rajkowski K, Griffiths W, Bodin K, Sjövall J, Baulieu EE (2008) Pregnenolone sulfate in the brain: a controversial neurosteroid. Neurochem Int 52:522–540. https://doi.org/10.1016/j.neuint.2007.08.022
5. Majewska MD, Mienville JM, Vicini S (1988) Neurosteroid pregnenolone sulfate antagonizes electrophysiological responses to GABA in neurons. Neurosci Lett 90:279–284. https://doi.org/10.1016/0304-3940(88)90202-9
6. Park-Chung M, Malayev A, Purdy RH, Gibbs TT, Farb DH (1999) Sulfated and unsulfated steroids modulate gamma-aminobutyric acidA receptor function through distinct sites. Brain Res 830:72–87. https://doi.org/10.1016/s0006-8993(99)01381-5
7. Wu FS, Gibbs TT, Farb DH (1991) Pregnenolone sulfate: a positive allosteric modulator at the N-methyl-D-aspartate receptor. Mol Pharmacol 40:333–336
8. Park-Chung M, Wu FS, Purdy RH, Malayev AA, Gibbs TT, Farb DH (1997) Distinct sites for inverse modulation of N-methyl-D-aspartate receptors by sulfated steroids. Mol Pharmacol 52:1113–1123. https://doi.org/10.1124/mol.52.6.1113
9. Meyer DA, Carta M, Partridge LD, Covey DF, Valenzuela CF (2002) Neurosteroids enhance spontaneous glutamate release in hippocampal neurons. Possible role of metabotropic sigma1-like receptors. J Biol Chem 277:28725–28732. https://doi.org/10.1074/jbc.M202592200
10. Hige T, Fujiyoshi Y, Takahashi T (2006) Neurosteroid pregnenolone sulfate enhances glutamatergic synaptic transmission by facilitating presynaptic calcium currents at the calyx of held of immature rats. Eur J Neurosci 24:1955–1966. https://doi.org/10.1111/j.1460-9568.2006.05080.x
11. Lee KH, Cho JH, Choi IS, Park HM, Lee MG, Choi BJ, Jang IS (2010) Pregnenolone sulfate enhances spontaneous glutamate release by inducing presynaptic Ca^{2+}-induced Ca^{2+} release. Neuroscience 171:106–116. https://doi.org/10.1016/j.neuroscience.2010.07.057
12. Ueda H, Inoue M, Yoshida A, Mizuno K, Yamamoto H, Maruo J, Matsuno K, Mita S (2001) Metabotropic neurosteroid/sigma-receptor involved in stimulation of nociceptor endings of mice. J Pharmacol Exp Ther 298(2):703–710
13. Vriens J, Owsianik G, Hofmann T, Philipp SE, Stab J, Chen X, Benoit M, Xue F, Janssens A, Kerselaers S, Oberwinkler J, Vennekens R, Gudermann T, Nilius B, Voets T (2011) TRPM3 is a nociceptor channel involved in the detection of noxious heat. Neuron 70:482–494. https://doi.org/10.1016/j.neuron.2011.02.051
14. Edvinsson L (2004) Blockade of CGRP receptors in the intracranial vasculature: a new target in the treatment of headache. Cephalalgia 24:611–622
15. Benemei S, Nicoletti P, Capone JG, Geppetti P (2009) CGRP receptors in the control of pain and inflammation. Curr Opin Pharmacol 9:9–14
16. Held K, Kichko T, De Clercq K, Klaassen H, Van Bree R, Vanherck JC, Marchand A, Reeh PW, Chaltin P, Voets T, Vriens J (2015) Activation of TRPM3 by a potent synthetic ligand reveals a role in peptide release. Proc Natl Acad Sci USA 112:E1363–E1372. https://doi.org/10.1073/pnas.1419845112
17. Bennett DL, Clark AJ, Huang J, Waxman SG, Dib-Hajj SD (2019) The role of Voltage-gated Sodium channels in Pain Signaling. Physiol Rev 99:1079–1151. https://doi.org/10.1152/physrev.00052.2017
18. Lai J, Porreca F, Hunter JC, Gold MS (2004) Voltage-gated sodium channels and hyperalgesia. Annu Rev Pharmacol Toxicol 44:371–397. https://doi.org/10.1146/annurev.pharmtox.44.101802.121627

19. England S, Bevan S, Docherty RJ (1996) PGE_2 modulates the tetrodotoxin-resistant sodium current in neonatal rat dorsal root ganglion neurones via the cyclic AMP-protein kinase a cascade. J Physiol 495:429–440. https://doi.org/10.1113/jphysiol.1996.sp021604
20. Gold MS, Levine JD, Correa AM (1998) Modulation of TTX-R I_{Na} by PKC and PKA and their role in PGE_2-induced sensitization of rat sensory neurons in vitro. J Neurosci 18:10345–10355. https://doi.org/10.1523/JNEUROSCI.18-24-10345.1998
21. Kang IS, Cho JH, Lee MG, Jang IS (2018) Modulation of tetrodotoxin-resistant Na^+ channels by Amitriptyline in dural afferent neurons. Eur J Pharmacol 838:69–77. https://doi.org/10.1016/j.ejphar.2018.09.006
22. Nakamura M, Jang IS (2021) Propranolol modulation of tetrodotoxin-resistant Na^+ channels in dural afferent neurons. Eur J Pharmacol 910:174449. https://doi.org/10.1016/j.ejphar.2021.174449
23. Nakamura M, Jang IS (2022) Contribution of tetrodotoxin-resistant persistent Na^+ currents to the excitability of C-type dural afferent neurons in rats. J Headache Pain 23:73. https://doi.org/10.1186/s10194-022-01443-7
24. Morais A, Qin T, Ayata C, Harriott AM (2023) Inhibition of persistent sodium current reduces spreading depression-evoked allodynia in a mouse model of migraine with aura. Pain 2023 164:2564–2571. https://doi.org/10.1097/j.pain.0000000000002962
25. Baulieu EE, Robel P (1990) Neurosteroids: a new brain function? J Steroid Biochem Mol Biol 37:395–403. https://doi.org/10.1016/0960-0760(90)90490-c
26. Compagnone NA, Mellon SH (2000) Neurosteroids: biosynthesis and function of these novel neuromodulators. Front Neuroendocrinol 21:1–56. https://doi.org/10.1006/frne.1999.0188
27. Mensah-Nyagan AG, Meyer L, Schaeffer V, Kibaly C, Patte-Mensah C (2009) Evidence for a key role of steroids in the modulation of pain. Psychoneuroendocrinology 34 Suppl 1S169–S177. https://doi.org/10.1016/j.psyneuen.2009.06.004
28. Percie du Sert N, Hurst V, Ahluwalia A, Alam S, Avey MT, Baker M, Browne WJ, Clark A, Cuthill IC, Dirnagl U, Emerson M, Garner P, Holgate ST, Howells DW, Karp NA, Lazic SE, Lidster K, MacCallum CJ, Macleod M, Pearl EJ, Petersen OH, Rawle F, Reynolds P, Rooney K, Sena ES, Silberberg SD, Steckler T, Würbel H (2020) The ARRIVE guidelines 2.0: updated guidelines for reporting animal research. Br J Pharmacol 177:3617–3624. https://doi.org/10.1111/bph.15193
29. Harriott AM, Gold MS (2009) Electrophysiological properties of dural afferents in the absence and presence of inflammatory mediators. J Neurophysiol 101:3126–3134. https://doi.org/10.1152/jn.91339.2008
30. Nakamura M, Jang IS (2018) Characterization of dural afferent neurons innervating cranial blood vessels within the dura in rats. Brain Res 1696:91–102. https://doi.org/10.1016/j.brainres.2018.06.007
31. Murase K, Ryu PD, Randic M (1989) Excitatory and inhibitory amino acids and peptide-induced responses in acutely isolated rat spinal dorsal horn neurons. Neurosci Lett 103:56–63. https://doi.org/10.1016/0304-3940(89)90485-0
32. Mameli M, Carta M, Partridge LD, Valenzuela CF (2005) Neurosteroid-induced plasticity of immature synapses via retrograde modulation of presynaptic NMDA receptors. J Neurosci 25:2285–2294. https://doi.org/10.1523/JNEUROSCI.3877-04.2005
33. Cheung G, Lin YC, Papadopoulos V (2023) Translocator protein in the rise and fall of central nervous system neurons. Front Cell Neurosci 17:1210205. https://doi.org/10.3389/fncel.2023.1210205
34. Fang F, Christian WV, Gorman SG, Cui M, Huang J, Tieu K, Ballatori N (2010) Neurosteroid transport by the organic solute transporter OSTα-OSTβ. J Neurochem 115:220–233. https://doi.org/10.1111/j.1471-4159.2010.06920.x
35. Coste B, Osorio N, Padilla F, Crest M, Delmas P (2004) Gating and modulation of presumptive $Na_V1.9$ channels in enteric and spinal sensory neurons. Mol Cell Neurosci 26:123–134. https://doi.org/10.1016/j.mcn.2004.01.015
36. Kobayashi K, Fukuoka T, Obata K, Yamanaka H, Dai Y, Tokunaga A, Noguchi K (2005) Distinct expression of TRPM8, TRPA1, and TRPV1 mRNAs in rat primary afferent neurons with adelta/c-fibers and colocalization with trk receptors. J Comp Neurol 493:596–606. https://doi.org/10.1002/cne.20794
37. Matsumoto RR, Bowen WD, Tom MA, Vo VN, Truong DD, De Costa BR (1995) Characterization of two novel sigma receptor ligands: antidystonic effects in rats suggest sigma receptor antagonism. Eur J Pharmacol 280:301–310. https://doi.org/10.1016/0014-2999(95)00208-3
38. Straub I, Mohr F, Stab J, Konrad M, Philipp SE, Oberwinkler J, Schaefer M (2013) Citrus fruit and fabacea secondary metabolites potently and selectively block TRPM3. Br J Pharmacol 168:1835–1850. https://doi.org/10.1111/bph.12076
39. Fleidervish IA, Gutnick MJ (1996) Kinetics of slow inactivation of persistent sodium current in layer V neurons of mouse neocortical slices. J Neurophysiol 76:2125–2130. https://doi.org/10.1152/jn.1996.76.3.2125
40. Magistretti J, Alonso A (1999) Biophysical properties and slow voltage-dependent inactivation of a sustained sodium current in entorhinal cortex layer-II principal neurons: a whole-cell and single-channel study. J Gen Physiol 114:491–509. https://doi.org/10.1085/jgp.114.4.491
41. Shu HJ, Zeng CM, Wang C, Covey DF, Zorumski CF, Mennerick S (2007) Cyclodextrins sequester neuroactive steroids and differentiate mechanisms that rate limit steroid actions. Br J Pharmacol 150:164–175. https://doi.org/10.1038/sj.bjp.0706973
42. Streit AK, Netter MF, Kempf F, Walecki M, Rinné S, Bollepalli MK, Preisig-Müller R, Renigunta V, Daut J, Baukrowitz T, Sansom MS, Stansfeld PJ, Decher N (2011) A specific two-pore domain potassium channel blocker defines the structure of the TASK-1 open pore. J Biol Chem 286:13977–13984. https://doi.org/10.1074/jbc.M111.227884
43. Bennett BD, Callaway JC, Wilson CJ (2000) Intrinsic membrane properties underlying spontaneous tonic firing in neostriatal cholinergic interneurons. J Neurosci 20:8493–8503. https://doi.org/10.1523/JNEUROSCI.20-22-08493.2000
44. Taddese A, Bean BP (2002) Subthreshold sodium current from rapidly inactivating sodium channels drives spontaneous firing of tuberomammillary neurons. Neuron 33:587–600. https://doi.org/10.1016/s0896-6273(02)00574-3
45. Cho JH, Choi IS, Lee SH, Lee MG, Jang IS (2015) Contribution of persistent sodium currents to the excitability of tonic firing substantia gelatinosa neurons of the rat. Neurosci Lett 591:192–196. https://doi.org/10.1016/j.neulet.2015.02.039
46. Bellingham MC (2011) A review of the neural mechanisms of action and clinical efficiency of riluzole in treating amyotrophic lateral sclerosis: what have we learned in the last decade? CNS Neurosci Ther 17:4–31. https://doi.org/10.1111/j.1755-5949.2009.00116.x
47. Gu N, Vervaeke K, Hu H, Storm JF (2005) Kv7/KCNQ/M and HCN/h, but not KCa2/SK channels, contribute to the somatic medium after-hyperpolarization and excitability control in CA1 hippocampal pyramidal cells. J Physiol 566:689–715. https://doi.org/10.1113/jphysiol.2005.086835
48. Mateos-Aparicio P, Murphy R, Storm JF (2014) Complementary functions of SK and Kv7/M potassium channels in excitability control and synaptic integration in rat hippocampal dentate granule cells. J Physiol 592:669–693. https://doi.org/10.1113/jphysiol.2013.267872
49. Mourre C, Fournier C, Soumireu-Mourat B (1997) Apamin, a blocker of the calcium-activated potassium channel, induces neurodegeneration of Purkinje cells exclusively. Brain Res 778:405–408. https://doi.org/10.1016/s0006-8993(97)01165-7
50. Horishita T, Ueno S, Yanagihara N, Sudo Y, Uezono Y, Okura D, Sata T (2012) Inhibition by pregnenolone sulphate, a metabolite of the neurosteroid pregnenolone, of voltage-gated sodium channels expressed in Xenopus oocytes. J Pharmacol Sci 120:54–58. https://doi.org/10.1254/jphs.12106sc
51. Horishita T, Yanagihara N, Ueno S, Sudo Y, Uezono Y, Okura D, Minami T, Kawasaki T, Sata T (2014) Neurosteroids allopregnanolone sulfate and pregnanolone sulfate have diverse effect on the α subunit of the neuronal voltage-gated sodium channels $Na_V1.2$, $Na_V1.6$, $Na_V1.7$, and $Na_V1.8$ expressed in xenopus oocytes. Anesthesiology 121:620–631. https://doi.org/10.1097/ALN.0000000000000296
52. Hains BC, Waxman SG (2007) Sodium channel expression and the molecular pathophysiology of pain after SCI. Prog Brain Res 161:195–203. https://doi.org/10.1016/S0079-6123(06)61013-3
53. Stafstrom CE (2007) Persistent sodium current and its role in epilepsy. Epilepsy Curr 7:15–22. https://doi.org/10.1111/j.1535-7511.2007.00156.x
54. Barbieri R, Bertelli S, Pusch M, Gavazzo P (2019) Late sodium current blocker GS967 inhibits persistent currents induced by familial hemiplegic migraine type 3 mutations of the SCN1A gene. J Headache Pain 20:107. https://doi.org/10.1186/s10194-019-1056-2

55. Rush AM, Waxman SG (2004) PGE_2 increases the tetrodotoxin-resistant $Na_V1.9$ sodium current in mouse DRG neurons via G-proteins. Brain Res 1023:264–271. https://doi.org/10.1016/j.brainres.2004.07.042
56. Maingret F, Coste B, Padilla F, Clerc N, Crest M, Korogod SM, Delmas P (2008) Inflammatory mediators increase $Na_V1.9$ current and excitability in nociceptors through a coincident detection mechanism. J Gen Physiol 131:211–225. https://doi.org/10.1085/jgp.200709935
57. Bonnet C, Hao J, Osorio N, Donnet A, Penalba V, Ruel J, Delmas P (2019) Maladaptive activation of $Na_V1.9$ channels by nitric oxide causes triptan-induced medication overuse headache. Nat Commun 10:4253. https://doi.org/10.1038/s41467-019-12197-3
58. Gada K, Plant LD (2019) Two-pore domain potassium channels: emerging targets for novel analgesic drugs: IUPHAR Review 26. Br J Pharmacol 176:256–266. https://doi.org/10.1111/bph.14518
59. Jensen TS, Finnerup NB (2014) Allodynia and hyperalgesia in neuropathic pain: clinical manifestations and mechanisms. Lancet Neurol 13:924–935. https://doi.org/10.1016/S1474-4422(14)70102-4
60. Jackson AC, Yao GL, Bean BP (2004) Mechanism of spontaneous firing in dorsomedial suprachiasmatic nucleus neurons. J Neurosci 24:7985–7998. https://doi.org/10.1523/JNEUROSCI.2146-04.2004
61. Xie RG, Zheng DW, Xing JL, Zhang XJ, Song Y, Xie YB, Kuang F, Dong H, You SW, Xu H, Hu SJ (2011) Blockade of persistent sodium currents contributes to the riluzole-induced inhibition of spontaneous activity and oscillations in injured DRG neurons. PLoS ONE 6:e18681. https://doi.org/10.1371/journal.pone.0018681
62. Wulff H, Castle NA, Pardo LA (2009) Voltage-gated potassium channels as therapeutic targets. Nat Rev Drug Discov 8:982–1001. https://doi.org/10.1038/nrd2983
63. Emery EC, Young GT, McNaughton PA (2012) HCN2 ion channels: an emerging role as the pacemakers of pain. Trends Pharmacol Sci 33:456–463. https://doi.org/10.1016/j.tips.2012.04.004
64. Diener HC, Dodick DW, Goadsby PJ, Lipton RB, Olesen J, Silberstein SD (2012) Chronic migraine–classification, characteristics and treatment. Nat Rev Neurol 8:162–171. https://doi.org/10.1038/nrneurol.2012.13
65. Krivoshein G, Tolner EA, Maagdenberg AVD, Giniatullin RA (2022) Migraine-relevant sex-dependent activation of mouse meningeal afferents by TRPM3 agonists. J Headache Pain 23:4. https://doi.org/10.1186/s10194-021-01383-8
66. de Peretti E, Mappus E (1983) Pattern of plasma pregnenolone sulfate levels in humans from birth to adulthood. J Clin Endocrinol Metab 57:550–556. https://doi.org/10.1210/jcem-57-3-550
67. Rustichelli C, Bellei E, Bergamini S, Monari E, Lo Castro F, Baraldi C, Tomasi A, Ferrari A (2021) Comparison of pregnenolone sulfate, pregnanolone and estradiol levels between patients with menstrually-related migraine and controls: an exploratory study. J Headache Pain 22:13. https://doi.org/10.1186/s10194-021-01231-9
68. Koverech A, Cicione C, Lionetto L, Maestri M, Passariello F, Sabbatini E, Capi M, De Marco CM, Guglielmetti M, Negro A, Di Menna L, Simmaco M, Nicoletti F, Martelletti P (2019) Migraine and cluster headache show impaired neurosteroids patterns. J Headache Pain 20:61. https://doi.org/10.1186/s10194-019-1005-0
69. Du X, Hao H, Yang Y, Huang S, Wang C, Gigout S, Ramli R, Li X, Jaworska E, Edwards I, Deuchars J, Yanagawa Y, Qi J, Guan B, Jaffe DB, Zhang H, Gamper N (2017) Local GABAergic signaling within sensory ganglia controls peripheral nociceptive transmission. J Clin Invest 127:1741–1756. https://doi.org/10.1172/JCI86812
70. Willcockson H, Valtschanoff J (2008) AMPA and NMDA glutamate receptors are found in both peptidergic and non-peptidergic primary afferent neurons in the rat. Cell Tissue Res 334:17–23. https://doi.org/10.1007/s00441-008-0662-0
71. Mavlyutov TA, Duellman T, Kim HT, Epstein ML, Leese C, Davletov BA, Yang J (2016) Sigma-1 receptor expression in the dorsal root ganglion: reexamination using a highly specific antibody. Neuroscience 331:148–157. https://doi.org/10.1016/j.neuroscience.2016.06.030

Publisher's Note